



HAL
open science

A submesoscale coherent vortex in the Ligurian Sea: From dynamical barriers to biological implications

Anthony Bosse, Pierre Testor, Nicolas Mayot, Louis Prieur, Fabrizio d'Ortenzio, Laurent Mortier, Hervé Le Goff, Claire Gourcuff, Laurent Coppola, Héloïse Lavigne, et al.

► To cite this version:

Anthony Bosse, Pierre Testor, Nicolas Mayot, Louis Prieur, Fabrizio d'Ortenzio, et al.. A submesoscale coherent vortex in the Ligurian Sea: From dynamical barriers to biological implications. *Journal of Geophysical Research. Oceans*, 2017, 122 (8), pp.6196 - 6217. 10.1002/2016JC012634 . hal-01621729

HAL Id: hal-01621729

<https://amu.hal.science/hal-01621729>

Submitted on 15 Feb 2021

HAL is a multi-disciplinary open access archive for the deposit and dissemination of scientific research documents, whether they are published or not. The documents may come from teaching and research institutions in France or abroad, or from public or private research centers.

L'archive ouverte pluridisciplinaire **HAL**, est destinée au dépôt et à la diffusion de documents scientifiques de niveau recherche, publiés ou non, émanant des établissements d'enseignement et de recherche français ou étrangers, des laboratoires publics ou privés.

**₁ A submesoscale coherent vortex in the Ligurian Sea:
₂ from dynamical barriers to biological implications**

Anthony Bosse^{1,2}, Pierre Testor², Nicolas Mayot³, Louis Prieur³, Fabrizio

D'Ortenzio³, Laurent Mortier^{4,2}, Hervé Le Goff², Claire Gourcuff^{5,2}, Laurent

Coppola³, H elo ise Lavigne⁶, Patrick Raimbault⁶

Corresponding author: A. Bosse, University of Bergen, Geophysical Institute, All egaten 70,
5007 Bergen, Norway (anthony.bosse@uib.no)

¹University of Bergen and Bjerknes

Abstract.

In June 2013, a glider equipped with oxygen and fluorescence sensors has been used to extensively sample an anticyclonic Submesoscale Coherent Vor-

Center for Climate Research, Geophysical
Institute, Allégaten 70, 5007 Bergen,
Norway.

²Sorbonne Universités (UPMC, Univ
Paris 06)-CNRS-IRD-MNHN, Laboratoire
LOCEAN, 4 place Jussieu, F-75005 Paris,
France.

³Sorbonne Universités (UPMC, Univ
Paris 06)-CNRS, Laboratoire
d’Océanographie de Villefranche, F-06230
Villefranche/mer, France.

⁴ENSTA Paristech, Palaiseau, France

⁵Euro-Argo ERIC, Brest, France

⁶Istituto Nazionale di Oceanografia e di
Geofisica Sperimentale - OGS, Trieste, Italy

⁷Aix-Marseille University, Sud Toulon-Var
University, CNRS/INSU, IRD, MIO,
Marseille, France

6 tex (SCV) in the Ligurian Sea (NW Mediterranean Sea). Those measurements
7 are complemented by full-depth CTD casts (T, S, Oxygen) and water sam-
8 ples documenting nutrients and phytoplankton pigments within the SCV and
9 outside. The SCV has a very homogeneous core of oxygenated waters between
10 300 m and 1200 m formed 4.5 months earlier during the winter deep con-
11 vection event. It has a strong dynamical signature with peak velocities at
12 700 m depth of 13.9 cm s^{-1} in cyclogeostrophic balance. The eddy has a small
13 radius of 6.2 km corresponding to high Rossby number of -0.45 . The vor-
14 ticity at the eddy center reaches $-0.8f$. Cross-stream isopycnic diffusion of
15 tracers between the eddy core and the surroundings is found to be very lim-
16 ited due to dynamical barriers set by the SCV associated with a diffusivity
17 coefficient of about $0.2 \text{ m}^2 \text{ s}^{-1}$. The deep core is nutrients-depleted with con-
18 centrations of nitrate, phosphate and silicate 13–18% lower than the rich sur-
19 rounding waters. However, the nutriclines are shifted of about 20–50 m to-
20 ward the surface thus increasing the nutrients availability for phytoplank-
21 ton. Chlorophyll-a concentrations at the deep chlorophyll maximum are sub-
22 sequently about twice bigger as compared to outside. Pigments further re-
23 veal the predominance of nanophytoplankton inside the eddy and an enhance-
24 ment of the primary productivity. This study demonstrate the important im-
25 pact of post-convective SCVs on nutrients distribution and phytoplankton
26 community, as well as on the subsequent primary production and carbon se-
27 questration.

1. Introduction

28 The northwestern Mediterranean Sea is one the few particular places of the world's
29 oceans, where intense atmospheric forcing combined to a weak ocean stratification allows
30 vertical mixing to reach depths (>1500 – 2000 m). This phenomenon is called open-ocean
31 deep convection and is of critical importance for the ventilation of the deep oceans and
32 has been studied since the 1970s (see *Marshall and Schott* [1999] for a review). It can be
33 divided into three main phases (that however overlap in space and time) [*MEDOC-Group*,
34 1970]: *the preconditioning* consisting in a basin-scale cyclonic circulation causing a doming
35 of isopycnals at its center; *the mixing phase*, which results from cold and dry winds blowing
36 over the preconditioned area leading to intense heat losses of the ocean and a deepening
37 of the mixed layer (typically several hundreds of watts per squared meter for a couple of
38 days [*Leaman and Schott*, 1991]); *the spreading phase* induced by the restratification of the
39 water column that occurs, when the intense heat losses cease (generally in early spring).
40 During this last phase, the mixed patch of convected waters breaks up into numerous
41 eddies by conversion of potential energy into kinetic energy through baroclinic instability
42 [*Gascard*, 1978; *Legg and Marshall*, 1993; *Visbeck et al.*, 1996; *Jones and Marshall*, 1997].
43 In particular, Submesoscale Coherent Vortices are formed [*McWilliams*, 1985]. They
44 are characterized by a small radius, subsurface peak velocities and an extended lifetime
45 (> 1 year). They were found to be involved in the large-scale spreading of newly-formed
46 deep waters toward the western Mediterranean Sea [*Testor and Gascard*, 2003, 2006], the
47 Greenland Sea [*Gascard et al.*, 2002] and the Labrador Sea [*Lilly and Rhines*, 2002]. In
48 the western Mediterranean Sea, this process has been recognized as being particularly

49 important: SCVs could transport 30–50% of the newly formed deep waters out of the
50 convective zone [*Testor and Gascard, 2006; Bosse et al., 2016; Damien et al., in revision,*
51 *this issue*], while another important part could be transported by the mean circulation
52 [*Send et al., 1996*].

53 The strong rotation of SCVs sets transport barriers that drastically reduce the lateral
54 exchanges between their deep core and the surrounding waters [*Rhines and Young, 1983;*
55 *Provenzale, 1999*]. As a consequence, they are therefore extremely efficient in transport-
56 ing physical and biogeochemical tracers characteristics of their generation site over long
57 distances [*D’Asaro, 1988; Testor and Gascard, 2003; Bower et al., 2013*]. As a conse-
58 quence, they can greatly impact the biogeochemical cycles at a local scale. For instance,
59 *Budéus et al. [2004]* reported a significant increase in the bacteria abundance at great
60 depths within a deep SCVs observed in the Greenland Sea. *Durrieu de Madron et al.*
61 *[2017]* reveal sediments being trapped within cyclonic SCVs in the NW Mediterranean
62 Sea. In oxygen depleted oceans, they have been identified as local spots for denitrification
63 [*Löscher et al., 2015; Karstensen et al., in review, 2016*] and habitat compression due to
64 their very low oxygen content [*Lachkar et al., 2016*]. Especially in tropical oceanic basins,
65 subsurface eddies can be tentatively be detected from space when combined with infrared
66 satellite images [*Klemas and Yan, 2014*], even though the surface expression of deep sub-
67 surface eddies is often small [*Ciani et al., 2015*]. In the Mediterranean Sea, as well as in
68 high latitude environment characterized by small deformation radii of 5–10 km, sampling
69 the fine scale of eddies remnant of wintertime convection is thus very challenging.

70 By allowing a relatively high horizontal resolution (distance between consecutive profiles
71 2–4 km), autonomous gliders could characterize the dynamics of post-convective SCVs of

72 about 10 km in diameter observed in the NW Mediterranean Sea [*Bosse et al.*, 2016].
73 Winter 2013 was an intense convective year that produced many vortical structures. In
74 this study, we analyze *in situ* observations collected during summer 2013 in the Ligurian
75 Sea by a research vessel and a glider in the same SCV. About 10 days after the first
76 survey by the R/V, the glider met by pure luck the same eddy around 30 km to the
77 southwest from the first observation. Both observations have very high similarities in
78 their vertical structure and are separated by a relative close distance in space and time in
79 coherence with the typical drift of SCVs. The intense sampling of the upper 1000 m by the
80 glider combined with full-depth CTD casts and water samples documenting the nutrients
81 concentrations, as well as phytoplankton pigments enable the first detailed study of such
82 a small-scale post-convective vortex.

2. Data and methods

2.1. Basin-scale cruise

83 Since 2010, sustained observations of the circulation and water properties are carried
84 out within the framework of the MOOSE project (NW Mediterranean Sea Observatory:
85 <http://www.moose-network.fr/>). The MOOSE-GE cruises aim at providing a yearly snap-
86 shot in summer of the open-ocean part of the basin with about 70–100 CTD stations. As
87 an important part of this integrated ocean observing system, gliders are also regularly
88 deployed in the whole sub-basin along repeated sections. The common key objective of
89 the MOOSE observatory is to monitor the deep waters formation in the Gulf of Lions in
90 order to assess its effect on biogeochemical cycles, and on the longer-term environmental
91 and ecosystemic trends and anomalies [*Durrieu de Madron et al.*, 2011].

92 The period 2012-2013 was a period of particular intense sampling with 6 basin-scale
93 surveys from July 2012 to September 2013 [*Estournel et al.*, accepted; *Testor et al.*, in
94 revision, this issue].

95 **Hydrographical data:** In February 2013, the DEWEX leg 1 was carried out in the
96 NW Mediterranean Sea [*Testor*, 2013]. With 75 CTD casts distributed over the whole
97 basin, it enables to get a precious picture of the winter deep convection at its climax (see
98 figure 1). In June-July 2013, 72 CTD stations have been collected during the MOOSE-
99 GE 2013 cruise [*Testor et al.*, 2013]. A profile revealed the presence of a subsurface
100 vortex in the Ligurian Sea (see figure 2). The conductivity, temperature and pressure
101 measurements during those two cruises have been performed using a Seabird SBE911+
102 CTD probe. The CT sensors have been calibrated by pre- and post-deployment laboratory
103 analysis. After calibration, the absolute accuracy of the measurements is 0.003 for the
104 salinity and 0.001°C for the temperature. These calibrated CTD casts provide a ground
105 truth for the autonomous underwater gliders.

106 **Lowered ADCP (LADCP):** During the MOOSE-GE 2013 cruise, the rosette was
107 carrying two RDI WH 300 khz LADCPs (up and down looking). 61 LADCP profiles were
108 processed with the LDEO V8b code based on the inversion method developed by *Visbeck*
109 [2002]. All profiles were inversed at 8 m vertical resolution using both instruments from
110 the surface to the bottom, navigation data from the CTD file and bottom track constraint
111 when available. Precision on horizontal velocities range from 2 to 4 cm s⁻¹ for all validated
112 profiles. Here, we use the LADCP profile carried within the eddy (leg 1, station 7).

113 **Dissolved oxygen:** The rosette was equipped with a SBE43 sensor for dissolved
114 Oxygen (DO), which has been calibrated before the cruises operation and after with

115 post-cruises manufacturer calibrations. After calibration, the absolute accuracy of the
116 measurements is about $5 \mu\text{mol kg}^{-1}$. In addition, Winkler titration have been performed
117 on board after seawater sampling. The measurements have been done each day (every 4–5
118 stations) and the SBE43 sensor has been cleaned after each CTD cast following the manu-
119 facturer recommendations [Janzen *et al.*, 2007]. Later on, the Winkler analysis have been
120 used to adjust the SBE43 raw data, as specified by the GO-SHIP group ([http://www.go-](http://www.go-ship.org/)
121 [ship.org/](http://www.go-ship.org/)).

122 **Nutrients:** Water samples for nitrate, nitrite, phosphate and silicic acid determina-
123 tion were collected from the Niskin bottles into 20 mL polyethylene flasks and immediately
124 poisoned with $10 \mu\text{g L}^{-1}$ mercuric chloride and stored for subsequent laboratory analy-
125 sis following Kirkwood [1992]. Nitrate (NO_3^-), phosphate (PO_4^{3-}) and silicate ($\text{Si}(\text{OH})_4$)
126 ions were analyzed in laboratory by standard automated colorimetric system using a Seal
127 Analytical continuous flow AutoAnalyser III according to Aminot and K  rouel [2007]. In-
128 house standards regularly compared to the commercially available products (OSIL) were
129 used to ensure the reproducibility of the measurements between the analyses.

130 **Dissolved Inorganic Carbon:** For C_T (or DIC) measurements, seawater sam-
131 ples were collected into washed 500 mL borosilicate glass bottles, and poisoned with
132 a saturated solution of HgCl_2 . At the end of the cruise, the samples were sent
133 to the SNAPO (Service National d'Analyse des Param  tres Oc  aniques du CO_2 :
134 <http://soon.ipsl.jussieu.fr/SNAPOCO2/>) for analysis. The measurements were performed
135 by potentiometric titration using a closed cell, as described in details in the handbook of
136 methods for the analysis of the various parameters of the CO_2 system in seawater [DOE,
137 1994]. The precisions obtained for these measurements are $2.2 \mu\text{mol kg}^{-1}$.

138 **Pigments:** The vertical distribution of phytoplankton pigment concentrations was
 139 determined through discrete water samples collected with Niskin bottles mounted on the
 140 CTD rosette. The discrete water samples were then filtered (GF/F) and High-Performance
 141 Liquid Chromatography (HPLC) analyses have been performed to provide a precise de-
 142 termination of the different phytoplankton pigments concentrations. All HPLC measure-
 143 ments used here were conducted at the Laboratoire d’Océanographie de Villefranche (see
 144 *Ras et al.* [2008] for details on the HPLC method). As in *Mayot et al.* [submitted, this
 145 issue], we used the pigment-based approach proposed by *Claustre* [1994] and further im-
 146 proved by *Vidussi et al.* [2001] and *Uitz et al.* [2006] to estimate the contribution of three
 147 phytoplankton size classes: micro-, nano-, and pico-phytoplankton (respectively, f_{micro} ,
 148 f_{nano} and f_{pico}) to the total phytoplankton biomass estimated as $[Chl_a]$ the chlorophyll-a
 149 concentration. Seven diagnostic pigments were selected as biomarkers of major phy-
 150 toplankton taxa: fucoxanthin ($[Fuco]$), peridinin ($[Perid]$), alloxanthin ($[Allo]$), 19’-
 151 butanoyloxyfucoxanthin ($[ButFuco]$), 19’-hexanoyloxyfucoxanthin ($[HexFuco]$), zeaxan-
 152 thin ($[Zea]$) and total chlorophyll-b (chlorophyll-b + divinyl chlorophyll-b = $[TChl_b]$) to
 153 compute f_{micro} , f_{nano} , and f_{pico} :

$$f_{micro} = (1.41[Fuco] + 1.41[Perid]) / \sum DPW \quad (1)$$

$$f_{nano} = (1.27[HexFuco] + 0.35[ButFuco] + 0.60[Allo]) / \sum DPW \quad (2)$$

$$f_{pico} = (1.01[TChl_b] + 0.86[Zea]) / \sum DPW \quad (3)$$

154 with $\sum DPW$ a weighted sum of the seven diagnostic pigments concentration: $DPW =$
 155 $(1.41[Fuco] + 1.41[Perid] + 1.27[HexFuco] + 0.35[ButFuco] + 0.60[Allo] + 1.01[TChl_b] +$
 156 $0.86[Zea])$. Eventually, the phytoplankton class-specific vertical profiles of chlorophyll-a
 157 were deduced by: $[Chl_a]_{class}(z) = [Chl_a](z)f_{class}(z)$.

158 **Primary production:** The phytoplankton primary production was estimated using
159 the bio-optical model described by *Morel* [1991]. The euphotic depth was determined from
160 vertical profiles of $[Chl_a](z)$ [*Morel and Berthon*, 1989; *Morel and Maritorena*, 2001] and
161 combined with the phytoplankton class-specific photophysiological properties determined
162 by *Uitz et al.* [2008] (see more details in *Mayot et al.* [submitted, this issue], supplementary
163 material S1). The model produces an estimate of the primary production associated with
164 each of the three phytoplankton size classes (P_{micro} , P_{nano} and P_{pico}).

2.2. Glider missions

165 Autonomous oceanic gliders are now an essential part of ocean observing techniques
166 [*Testor et al.*, 2010]. They sample the ocean along a saw-tooth trajectory between the
167 surface and 1000 m. The typical slope of isopycnals are much smaller than the pitch angle
168 of the glider (about ± 15 – 25°), so dives and ascents can be considered as vertical profiles
169 and are separated by typically 2–4 km and 2–4 h depending on the sampling strategy
170 (dives only, or dives/ascents). Having a horizontal speed of 30–40 km per day, they are
171 perfectly suited to sample oceanic features like eddies that propagate slower [*Martin et al.*,
172 2009; *Frajka-Williams et al.*, 2009; *Bouffard et al.*, 2010, 2012; *Fan et al.*, 2013; *Pelland*
173 *et al.*, 2013; *Bosse et al.*, 2015, 2016; *Cotroneo et al.*, 2015; *Thomsen et al.*, 2016]. In the
174 framework of the MOOSE project, gliders are deployed on a regular basis and in particular
175 along the Nice–Calvi section crossing the Ligurian Sea [*Bosse et al.*, 2015]. Here, we use
176 two deployments of Slocum gliders along this endurance line: the mission MOOSE T00–23
177 in January–March and MOOSE T00–26 in June–July 2013.

178 **Hydrographical data:** The gliders were equipped with an unpumped Seabird
179 SBE41CP CTD probe. Direct comparisons with calibrated shipborne CTD measure-

180 ments could be done for both deployments following the approach used in *Bosse et al.*
181 [2015, 2016]. For the summer mission (MOOSE T00–26), we refined the calibration by
182 adjusting the glider data on the calibrated CTD inside the SCV core. Given the very
183 homogeneous SCV core, both platform agree very well: the root mean square (RMS)
184 difference between 600 and 800 m depth inside the SCV of 0.002°C in temperature and
185 0.001 in salinity, which is comparable with the shipborne CTD accuracy. In addition, ther-
186 mal lag effects of the probe that can affect salinity measurements in the strong summer
187 thermocline have been corrected following *Garau et al.* [2011].

188 **Depth-average currents:** From their dead reckoning navigation and GPS fixes made
189 at the surface, gliders deduce a mean current. This latter represents the mean current
190 over each dive and will hereafter be referred as the depth-average currents (DAC). A
191 compass calibration has been carried out before each deployment allowing DAC to be
192 used to reference geostrophic velocities as commonly done (see for instance the previously
193 cited literature).

194 **Dissolved oxygen:** The gliders were equipped with an Anderraa Optode 3835. The
195 raw phase measurements were corrected from a sensor time response estimated by compar-
196 ing measurements of consecutive up and down profiles. Time delays of 30 s (MOOSE T00–
197 23) and 25 s (MOOSE T00–26) were estimated, the same order of magnitude than the
198 25 s provided by the manufacturer. Oxygen concentration was then computed using the
199 corrected phase measurements and temperature measurements from the CTD, following
200 the Argo recommendations [*Thierry and Bittig*, 2016]. As a final calibration step, an
201 offset (respectively 10.0 and $20.3 \mu\text{mol kg}^{-1}$ for the missions MooseT00-23 and T00-26)
202 and a slope (respectively 0.016 and $-0.0049 \mu\text{mol kg}^{-1} \text{ m}^{-1}$) were least squares fitted in

203 order to minimize the difference between the glider optode and calibrated shipborne mea-
204 surements. The comparison is made with CTD casts carried out at less than 50 km and
205 2 days apart from glider measurements for the winter mission and with profiles carried out
206 in the SCV core for the summer deployment. After this calibration procedure the RMS
207 difference between the glider and shipborne measurements at depth was respectively 1.5
208 and $1.3 \mu\text{mol kg}^{-1}$, which is below the accuracy of absolute shipborne measurement.

209 **Chl-a Fluorescence:** The glider also had a Wet Labs bio-optical fluoremeter. Un-
210 fortunately, no direct comparison with HPLC measurements was possible with the glider
211 data, as the short response time of phytoplankton growth imposes a very close match-up in
212 space and time. Alternatively, a calibration method using satellite ocean color was applied
213 [*Lavigne et al.*, 2012]. In this calibration step, fluorescence profiles were also corrected for
214 non-photochemical quenching following *Xing et al.* [2012]. With a larger dataset, *Mayot*
215 *et al.* [in revision, this issue] tested this method against bottle measurements. Both cal-
216 ibrations gave satisfying and similar results (Mean Absolute Deviation Percent of 23%
217 with HPLC and 38% with satellite), thus supporting the use of the method of *Lavigne*
218 *et al.* [2012] when direct comparison with *in situ* data is not possible.

2.3. Remote sensing

219 Surface chlorophyll concentration from level 2 MODIS Aqua product (daily and at 1 km
220 resolution) were extracted over the northwestern Mediterranean Sea from the NASA web
221 site (<http://oceancolor.gsfc.nasa.gov/>). All the MODIS L2 flags have been applied.

2.4. SCV reconstruction

2.4.1. Vortex center detection

223 As in *Bosse et al.* [2015, 2016], glider depth-average currents are used to retrieve the
224 eddy velocity field. A mean advection is estimated by low-passing the along-track DAC
225 using a Gaussian moving average of 35 km variance. The eddy center detection method is
226 then applied on the DAC minus the local advection. In order to find the the eddy center,
227 the following cost function is minimized: $g(x, y) = 1/n \sum_{i=1}^n [\mathbf{v}_i \cdot \mathbf{r}_i(x, y) / \|\mathbf{r}_i(x, y)\|]^2$ with
228 (x, y) a given position in the horizontal plane, $\mathbf{r}_i(x, y) / \|\mathbf{r}_i(x, y)\|$ the normalized vector
229 linking (x, y) to the location where the depth-average velocities \mathbf{v}_i are estimated. We
230 choose $n = 4$ centered around each vortex center to preserve the synoptic character of
231 the sampling (see figure 7 in *Bosse et al.* [2015] for an illustration of this cost function
232 method).

233 The SCV center is thus detected five times from June 26 to July 4, 2013 (see figure 2-c).
234 During that time period, 106 glider profiles and 59 DACs were carried out at less than
235 20 km of the eddy center. Every profile could then be positioned in the eddy coordinate
236 framework in order to reconstruct its dynamics (see figure 3).

237 **2.4.2. Objective mapping**

238 Full-depth shipborne CTD cast were collected inside the eddy core and outside (see
239 figure 2). Those profiles provide useful informations below 1000 m, the maximum sampling
240 depth of the glider. In order to map the eddy properties (θ , S_P and DO) down to the sea
241 floor at about 2500 m, an objective mapping was performed with a spatial decorrelation
242 scale of 6.3 km in the radial and 800 m in the vertical axis (see figure 4) [*Bretherton et al.*,
243 1976; *Le Traon*, 1990]. This radial scale results from the eddy radius deduced from the
244 DACs (see caption of figure 3-c) and the vertical scale corresponds to the thickness of
245 the homogeneous core. To perform this analysis, we used all the glider profiles in the top

1000 m and only two full-depth shipborne profiles below. The shipborne CTD cast within
the core was positioned at $r = 3.8$ km from the eddy center by fitting the mean LADCP
velocity of the 0–1000 m layer (11.0 cm s^{-1}) to the glider DACs (see figure 3-c). And
the profile representative of the background, taken as the mean profile observed in the
Ligurian Sea during the MOOSE-GE cruise (see figure 2-b), was positioned at $r = 20$ km
(more than three eddy radius).

Objective mapping of potential temperature was also performed in the horizontal plane
and in the eddy coordinate system (see figure 3-a). For these interpolations, an isotropic
decorellation scale of 6.3 km has simply been used.

2.4.3. Eddy dynamics in gradient wind balance

Small scale vortices are generally characterized by a relatively strong horizontal shear ($>$
 $0.1f$). Their force balance are thus ageostrophic and the centrifugal force needs to be taken
into account, otherwise the velocity are underestimated for anticyclones and overestimated
for cyclones [*Elliott and Sanford, 1986; Penven et al., 2014; Bosse et al., 2015, 2016*]. The
cyclostrophic velocities v_c can be retrieved by solving the quadratic equation expressing the
gradient wind balance in a cylindrical coordinate system: $v_c^2(r, z)/r + fv_c(r, z) = fv_g(r, z)$
with r the distance to the eddy center, z the depth, f the Coriolis parameter and v_g the
geostrophic velocity field. Keeping the relevant solution from this equation then yields:

$$v_c(r, z) = \frac{rf}{2} \left(-1 + \sqrt{1 + \frac{4v_g(r, z)}{rf}} \right) \quad (4)$$

The negative root of the quadratic equation is excluded as it corresponds to non-stable
solutions with vorticity below $-f$. Note that this equation can be solved only if the
geostrophic shear is not too strongly anticyclonic (i.e. $4v_g(r, z)/rf < -1$). As expected,

267 the amplitude of cyclogeostrophic velocities are smaller (respectively larger) than v_g for
268 cyclones (resp. anticyclones). To infer cyclostrophic velocities, absolute geostrophic
269 velocities have thus to be determined first.

270 Classically, the cross-track geostrophic vertical shear is computed by integrating the
271 thermal wind balance from a smoothed density section. Here, we applied a Gaussian
272 moving average of 3.2 km variance (half of the eddy radius) to the analyzed density field to
273 filter out residual small-scale isopycnals variability without fading the SCV signature. The
274 cut-off length scale is set in accordance with the vortex radius. A modal decomposition
275 on typical density profiles consistently yields a first baroclinic deformation radius of about
276 6 km. This is relatively small compared to other oceans owing to the low stratification of
277 the northwestern Mediterranean Sea.

278 For a Gaussian geopotential anomaly, the orbital velocities of the SCV can be written
279 as: $V(r) = V_0 \frac{r}{r_0} e^{-[(\frac{r}{r_0})^2 - 1]/2}$ where V_0 corresponds to the velocity maximum located at
280 the distance r_0 from the center [McWilliams, 1985; Pingree and Le Cann, 1993]. We
281 performed a least squares fit of this Gaussian model to the total DAC from the glider
282 in order to estimate V_0 ($= 12.2 \pm 2.2 \text{ cm s}^{-1}$) and r_0 ($= 6.3 \pm 0.2 \text{ km}$). Observations
283 and parametrized velocity show a good agreement with velocities decreasing close to zero
284 within about three radii (see figure 3-b).

285 Then, the geostrophic component of total depth-average currents is computed following
286 Bosse *et al.* [2016], so the geostrophic shear can be correctly referenced from the surface to
287 1000 m depth (see details in appendix of the latter reference). This method applies when
288 ageostrophy is due to the centrifugal force, which is particularly relevant for small-scale

289 SCVs. The geostrophic component is about 20% smaller in magnitude than total ones
 290 (9.8 cm s⁻¹ vs 12.2 cm s⁻¹).

291 And finally, cyclostrophic velocities are inferred using (4). If the geostrophic shear is
 292 directly referenced without removing the cyclostrophic component, the geostrophic shear
 293 becomes too intense for equation (4) to be solved (i.e. $4v_g(r, z)/rf < -1$).

294 Note that isopycnal slope below 1000 m is constrained by only two profiles, one rep-
 295 resentative of the core and the other of the background. Subsequent errors in the eddy
 296 velocity field can thus be the result of miscalculating geostrophic shear. The velocity field
 297 shown in figure 5-a still fall into the confidence range of LADCP measurements over the
 298 whole water column. They seem to be slightly underestimated close to the surface. The
 299 RMS difference is 1.9 cm s⁻¹, which is satisfactory smaller than the LADCP accuracy
 300 (mean error of 3.1 cm s⁻¹ in velocity amplitude).

301 2.4.4. Complementary diagnostics

302 **Vorticity, strain:** We computed the relative vorticity from the radial distribution of
 303 cyclogeostrophic velocities $v_c(r, z)$: $\zeta(r, z) = \nabla \times \mathbf{v}(r, z) = r^{-1}\partial_r(rv_c) = v_c/r + \partial_r v_c$, as
 304 well as the strain rate: $\eta(r, z) = \partial_r v_c - v_c/r$. It expresses the rate at which adjacent fluid
 305 parcels will separate under the action of the flow.

306 **Potential vorticity:** The Ertel's Potential Vorticity (PV, in m⁻¹ s⁻¹) is: $q \equiv$
 307 $-\zeta_a \cdot \nabla \sigma / \rho_0$ where $\zeta_a = (\zeta + f)\hat{z}$ is the absolute vorticity. In the ocean interior (i.e. away
 308 from surface and bottom boundaries), the fluid is governed by the inviscid Boussinesq
 309 equations and this quantity is conservatively advected [*Ertel*, 1942]. In non-frontal regions
 310 where lateral density gradients are small, the PV can be written as: $q(r, z) = fN(r, z)^2(1+$
 311 $Ro(r, z))/g$.

2.5. Lateral isopycnic diffusion

312 The glider collected a remarkable number of profiles (106 at less than 20 km of the
313 center). The glider has sampled the SCV for about 10 days, which is certainly not long
314 enough to measure an evolution of its core. Nonetheless, as we have a good estimate
315 of its age, a lateral eddy diffusion coefficient K_ρ can be fitted to the radial distribution
316 of tracers observed along isopycnals across the eddy core. We assume an step-like initial
317 tracer distribution and then solve the diffusion equation in cylindrical coordinates (details
318 are given in appendix A). This model describes the evolution under radial diffusion of
319 a cylinder (radius L) with initial concentration T_0 located in an infinite environment of
320 tracer concentration T_∞ . The cylinder (representing the SCV) then progressively loses
321 its anomalous concentration until reaching T_∞ .

322 In order to compute K_ρ , some parameters have to be specified. L the radius of the
323 initial tracer distribution is chosen as $\sqrt{2} \simeq 1.41$ eddy radius. This is where vorticity of
324 a Gaussian vortex changes sign. This is also in good agreement with the observed tracer
325 distribution (see figure 6-a). T_∞ the concentration of the surrounding waters is taken
326 as the average between L and 20 km. T_0 is optimized along with K_ρ in order for the
327 theoretical profile to fit to observations. By doing this, we allow the tracer concentration
328 to slightly vary at the top and the base of the core, where vertical diffusion can also be
329 at play and would act rather homogeneously within the eddy core.

330 The analysis is here conducted for θ , S_P and DO (see figure 6-a). DO can be considered
331 as a passive tracer below the euphotic layer due to the very low biological activity in
332 absence of sunlight. Dissolved oxygen is probably the most suited tracer, as it exhibits
333 important and consistent lateral gradient across the SCV rim, while temperature and

334 salinity gradients vanish close to its equilibrium depth making diffusion estimate impos-
335 sible. However, it remains uncertain if the SCV has an effect on the bacterial activity as
336 shown by *Budéus et al.* [2004]. If it is the case, DO might not be as conservative as it
337 normally is.

338 **Model validity:** Such an approach assumes (1) the vertical diffusion is small com-
339 pared to horizontal one, and (2) the initial distribution is a step. *McWilliams* [1985]
340 gave roughly similar horizontal and vertical diffusivity coefficient for a typical subsurface
341 SCV. Subsequent fluxes should then be mainly controlled by the tracer gradients. The
342 first point is thus valid within the SCV core between 350 m and 1000 m, where vertical
343 gradients of tracers are very weak (at least one order of magnitude smaller than horizontal
344 ones). The second point is a simplification that would likely cause an overestimation of
345 the diffusivity coefficients. During the dynamical adjustment occurring at the early stage
346 of the SCV's life, sharp gradients will indeed be rapidly smoothed [*McWilliams*, 1988].

3. Results

3.1. Water mass transformation during winter 2013

3.1.1. Basin-scale context

348 There are three main water masses in the Western Mediterranean Sea [*Millot*, 1999].
349 The fresh (< 38.5) and warm ($> 15^{\circ}\text{C}$) Atlantic Waters (AW) found in the surface layers
350 (100–200 m in the basin center and deeper along continental slope due to the boundary
351 circulation, see figure 1-c and 2-c). The warm and salty layer of Levantine Intermediate
352 Waters (LIW) at intermediate depths (200–800 m). This water mass is formed in the
353 Eastern Mediterranean Sea and further spread toward the Western Mediterranean Sea
354 through the Sicily channel. Due to their relatively "old" age, they are characterized by an

355 oxygen minimum when they reach the Western Mediterranean Sea (see figure 1-d and 2-d).
356 The Western Mediterranean Deep Waters (WMDW) eventually fill the rest of the water
357 column to the bottom. Due to its relative small overturning timescale, the Mediterranean
358 Sea is highly sensitive to climate change [*Somot et al.*, 2006]. The heat and salt contents
359 of the deep waters have been gradually increasing during the last decades [*Béthoux et al.*,
360 1990; *Krahmann and Schott*, 1998], with step-like events caused by major deep convection
361 events [*Schroeder et al.*, 2016; *Houpert et al.*, 2016].

362 In addition to AW, LIW and WMDW, other less widespread water masses are found.
363 The Winter Intermediate Waters (WIW), which result from intermediate mixing down
364 to about 300 m maximum (above the LIW layer) in open-ocean [*Gasparini et al.*, 2005]
365 or in shelf areas of the Gulf of Lions [*Juza et al.*, 2013] or the Catalan Sea [*Vargas-
366 Yáñez et al.*, 2012]. They are classically characterized by potential temperature below
367 13°C. Recently, *Bosse et al.* [2016] introduced an additional water mass to complete this
368 picture. Intermediate mixing can indeed result in the episodic formation intermediate
369 waters below the LIW layer at about 500 to 1000 m depth. This water mass lies deeper
370 than WIW and is also much warmer ($> 13^{\circ}\text{C}$) and saltier (> 38.5), as a result of the
371 mixing of the elevated heat and salt contents of the LIW layer. It has been called Winter
372 Deep Waters (WDW). Favorable conditions to its formation were observed in 2012 and
373 2013 in the Ligurian Sea [*Bosse et al.*, 2016], as well as in 2014 and 2015 in the Gulf of
374 Lions [*Bosse*, 2015].

375 **3.1.2. Winter mixing in the Ligurian Sea**

376 The glider mission MOOSE T00–23 sampled the Ligurian Sea from January to March
377 at the climax of the deep convection. The figure 1-c shows the progressive deepening

378 of the mixed layer (defined using the refined criterion of *Houpert et al.* [2016]). As seen
379 by the glider along the Nice–Calvi section, the mixed layer reaches a maximum depth of
380 about 800 m between the 13th and 16th of February (see figure 1-c). Shipborne CTD casts
381 were taken along the same section a few days later on February 19 and 20, while surface
382 layers had already started to restratify after an intense wind event. However, CTD casts
383 collected slightly southwest of the glider section revealed comparable deep mixed layers.
384 This illustrates the high spatial and temporal variability of the convective area. The
385 center of the Ligurian Sea convective zone could have been located slightly southwest of
386 the Nice–Calvi glider section, as also suggested by satellite images (see figure 8 in *Houpert*
387 *et al.* [2016]).

388 In terms of hydrographical characteristics, when the mixed layer was observed deeper
389 than 600 m, it was characterized by a mean potential temperature close to 13.17°C and
390 practical salinity close to 38.54. In a θ/S diagram, this water mass lies on the mixing line
391 between LIW and WMDW and can be qualified as Winter Deep Waters following *Bosse*
392 *et al.* [2016]. The mixed layer was observed to be deeper than 600 m in the Gulf of Lions
393 and characterized by colder and fresher characteristics of the newly formed WMDM (see
394 figure 1-b).

3.2. SCV characteristics

3.2.1. Hydrographical description

396 During the MOOSE-GE 2013 cruise, a CTD cast carried out in the Ligurian Sea on
397 June 15 revealed a particularly homogeneous layer of oxygenated waters between 300 m
398 and 1200 m depth ($\theta \sim 13.18^\circ\text{C}$, $S_P \sim 38.54$, $\text{DO} = 195\text{--}200 \mu\text{mol kg}^{-1}$, see figure
399 2-b). Shortly after, a glider deployed along the repeated "Nice–Calvi" endurance line

400 (mission MOOSE T00–26) crossed by chance the same water mass (see figure 2-c). From
401 600 to 900 m, potential temperature only increases by 0.0014° and salinity by 0.0015.
402 The resulting vertical stratification is very weak: $+0.0005 \text{ kg m}^{-3}$ from 600 m to 900 m
403 and roughly constant potential density from 750 to 900 m (equivalent to $N \sim f$). This
404 low stratified water is enclosed within an anticyclonic rotation. The deep isopycnals
405 deformation is characteristics of Submesoscale Coherent Vortices (SCV) with a doming of
406 isopycnals above its equilibrium depth and a deepening below it [McWilliams, 1985]. The
407 presence of ventilated waters at such depths indicates a recent origin related to winter
408 mixing. Figure 7 shows on a salinity oxygen space the clear signature of the SCV between
409 300 and 1200 m. At the base of the core between 1200 and 1800 m, the oxygen content
410 is lower than the surroundings and remarkably homogeneous. As described before, the
411 convective area had about the same θ/S_P characteristics as the SCV around mid-February
412 in the Ligurian Sea. This would indicate the SCV was formed about 4.5 month prior to
413 its sampling during summer.

414 The SCV has a clear signature on heat, salt and oxygen distribution over the water
415 column. At intermediate depths where LIW are usually found, the SCV core has a lower
416 temperature (-0.15°C) and salinity (-0.03). But, the more important signal is the clear
417 increase of the temperature (up to $+0.2^\circ\text{C}$) and salinity (up to $+0.05$) between 700 m and
418 1800 m. In terms of oxygen, it has a positive anomaly at all depths reaching $17 \mu\text{mol kg}^{-1}$
419 at the LIW level characterized by low oxygen concentrations. In the deep layers below
420 1700 m, salinity is systematically smaller than the surroundings with salinities of 38.48.
421 This value is typical of the WMDW observed prior to the intense production of saltier
422 deep waters during winter 2013 [Houpert et al., 2016; Testor et al., in revision, this issue].

423 The SCV would impact the whole water column down to the bottom, likely due to its
424 important barotropic rotation able to trap old deep waters during its formation.

425 Interestingly, quite marked LIW are found in the rim of the eddy ($\theta \sim 13.45^\circ\text{C}$ and $S \sim$
426 38.59) compared to typical values found in the Ligurian Sea (see figure 4). Figure 3-a shows
427 the potential temperature at 400 m in an eddy-centered frame where every observation has
428 been rotated according to its orbital velocity and observation date. This horizontal view
429 shows the heterogeneity of the LIW temperature at the rim of the eddy, unlike the very
430 homogeneous core (see figure 3-b, left panel). Some profiles located between one and two
431 radius reveal temperature reaching 13.61°C and salinity up to 38.63 . Such values are only
432 found along the continental slope off Corsica (see figure 2-c), the boundary circulation
433 along Sardinia and Corsica being known as a major inflow of warm and salty LIW to the
434 NW Mediterranean Sea [Millot, 1987; Bosse et al., 2015]. The SCV would have recently
435 been interacting with this LIW vein without being affected, as the core remains very
436 homogeneous while parts of the LIW vein have clearly been extracted and exported to
437 the open-sea.

438 3.2.2. Dynamical description

439 **Cyclogeostrophic velocities:** They show a clear maximum $V^{max} = 13.9 \pm 2.0 \text{ cm s}^{-1}$
440 at $R = 6.2 \pm 0.2 \text{ km}$ from the center. The peak velocity is found at 700 m depth where
441 the geostrophic shear (i.e. isopycnals slope) changes sign (see figure 5-a). Close to the
442 surface, velocities are significantly smaller (about 4 cm s^{-1} at the surface, 7 cm s^{-1} at
443 100 m) supported by LADCP measurements. Baroclinic velocities account for about 20%
444 of the total velocities, the rotation of this SCV appears to be mainly barotropic. This
445 could be the reason why the SCV also has a signature in the deep waters below its oxygenated

446 core. Ageostrophic cyclotrophic velocities reach 3.8 cm s^{-1} at a radial distance of 4.1 km
 447 smaller than the eddy radius. Ageostrophy is maximum at the origin and represents from
 448 about 10% at the surface up to $\sim 45\%$ around 700 m (see figure 5-a, right panel). This
 449 confirms the important role of centrifugal effects in the balance of small-scale SCVs.

450 **Rossby Number:** When normalized by the planetary vorticity f , the vorticity $\zeta(r, z)$
 451 represents a local Rossby number $Ro_l(r, z)$ that quantifies the non-linearity of the flow.
 452 Due to its small radius and intense orbital velocities, the relative vorticity of the SCV
 453 reaches pretty high values of $-0.80f$ at the eddy core, close to $-f$ the limit set by inertial
 454 instability for barotropic vortices [*Kloosterziel et al.*, 2007]. This value is very similar to
 455 $-0.85f$ reported by *Prater and Sanford* [1994] in a small Meddy in the Atlantic. Flow
 456 with large Rossby number close to unity are qualified as submesoscale flows, as they
 457 are not completely in geostrophic balance (see a recent review by *McWilliams* [2016] for
 458 more details). The Rossby number of the SCV, estimated at the velocity maximum as
 459 $Ro \equiv 2V^{max}/Rf$, ends up to be -0.45 ± 0.08 , comparable to previous estimates associated
 460 with post-convective SCVs in the NW Mediterranean Sea [*Testor and Gascard*, 2006;
 461 *Bosse et al.*, 2016]. *McWilliams* [1985] suggested that SCVs can survive interactions with
 462 external flows characterized by weaker horizontal shear. Here, the high vorticity of the
 463 SCV could make it survive interactions with boundary flows mostly in geostrophic balance
 464 (horizontal shear of about $0.1f$ or smaller). This also provides a rational explanation for
 465 the presence of the warm and salty LIW observed at the rim of the eddy that could result
 466 from its interaction with the LIW flow off Corsica (see figure 4 and 3).

467 **Burger Number:** The horizontal scale of oceanic eddies is controlled by the internal
 468 deformation radius: $R_d \equiv NH/f$ depending on H its vertical extension and N the water

469 column stratification ($N^2 \equiv -g\partial_z\sigma/\rho_0$). The stratification generally decreases with depth:
 470 here $N \leq 5f$ below 500 m (see figure 5-c). This explains why subsurface eddies have a
 471 small radius compared to surface mesoscale eddies. The Burger number further quantifies
 472 the ratio of the deformation radius to the eddy radius: $Bu \equiv [NH/fR]^2 = [R_d/R]^2$.
 473 To compute the Burger number of the SCV, $H = 1600$ m is defined from the vertical
 474 extension of its geopotential anomaly at the center (i.e. larger than 20% of its maximum
 475 value at 700 m) and $N = (4.0 \pm 0.4)f$ is the mean background stratification between 600
 476 and 800 m. This yields a Burger number of 1.14 ± 0.22 , close to unity. In a low stratified
 477 ocean, eddies have thus an unusual high aspect ratio ($R/H \sim N/f \in [1 : 10]$). This is
 478 a particular feature shared by many SCVs observed around the world's oceans [*D'Asaro,*
 479 *1988; Timmermans et al., 2008; Bower et al., 2013; Pelland et al., 2013; Bosse et al., 2015*],
 480 which can be theoretically explained in an idealized case [*Carpenter and Timmermans,*
 481 *2012*].

482 **Effect on stratification and potential vorticity:** The vertical stratification is
 483 significantly weakened inside the SCV almost to a factor of 2 with a mean value $2.4f$
 484 at ~ 700 m (see figure 5-c). Although there are few deep observations, the stratification
 485 increases close to the bottom, as observed at the base of deep anticyclonic SCVs [*Bosse*
 486 *et al., 2016*]. Combined with the strong negative vorticity, the PV is notably reduced up
 487 to a factor of 20 inside the core at the depth of the vorticity maximum and minimum
 488 of stratification. The PV reaches values as low as 10^{-13} m s $^{-1}$, which is one order of
 489 magnitude smaller than that of LIW SCVs formed by topographic interaction in the NW
 490 Mediterranean Sea [*Bosse et al., 2015*]. The PV conservation between an initial resting
 491 water parcel and the final rotating state enables to compute the initial stratification of

492 the resting fluid parcel: $N_{ini} = N_{scv} \sqrt{1 + Ro_l(0, 700)} = 1.1f$. Such a low value confirms
493 that convective processes might be at the origin of the SCV.

3.3. Dynamical barriers

494 By resolving the diffusion equation, a lateral isopycnic diffusion coefficient could be
495 estimated for each tracer at different depths (see figure 6). Around to the velocity max-
496 imum between 550 m and 800 m, the lateral gradient of temperature and salinity is too
497 weak and no estimation is possible. Where it can be estimated, K_ρ is $0.22 \pm 0.04 \text{ m}^2 \text{ s}^{-1}$.
498 The tracer distribution reaches background values at the radial distance of about $\sqrt{2}r_0$
499 ($= 8.9 \text{ km}$), where the relative vorticity becomes positive. This is also where the strain
500 rate is maximum (see figure 5-b). The dynamical barriers of the SCV seem to start there
501 and extend to the eddy center.

502 As explain in section 2.5, dissolved oxygen is the only tracer that provides K_ρ estimates
503 near the equilibrium depth of the SCV, where the horizontal vertical processes might be
504 the smallest. There is consistent values among the different tracers, except below the
505 core, where oxygen diffusivity seems to slightly diverge. This could be the effect of unknown
506 biological processes acting on the oxygen budget of the SCV. Indeed, *Budéus et al.* [2004]
507 showed a stimulation of the bacterial activity in a deep convective SCVs observed in the
508 Greenland Sea. However, this idea remains hard to verify here without dedicated mea-
509 surements. Furthermore, the base of the SCV's core is a region of stronger stratification
510 and where trapped near-inertial waves could enhance turbulence levels [*Kunze et al.*, 1995;
511 *Sheen et al.*, 2015]. Diapycnal mixing could then increase there, pushing to the limit our
512 simple 1D diffusion model. Again, with no turbulence measurements, we can unfortu-

513 nately not test this idea. Overall, all estimates agree on the order of magnitude of the
514 diffusion coefficient of $0.2 \text{ m}^2 \text{ s}^{-1}$.

515 *Okubo* [1971] reviewed estimates of the horizontal eddy diffusivity coefficient associated
516 with oceanic turbulence and its scale dependency ranging $1\text{--}100 \text{ m}^2 \text{ s}^{-1}$ for scales of 1--
517 100 km (see also a nice and more recent review in introduction of *Nencioli et al.* [2013]).
518 Here, we quantified the integral effect of unresolved small-scale processes on the erosion
519 of the SCV's core. This has been previously done for Meddies in the Atlantic Ocean:
520 *Hebert et al.* [1990] found a lateral eddy coefficient of $5 \text{ m}^2 \text{ s}^{-1}$ associated with the decay
521 of a 20 km radius Meddy and *McWilliams* [1985] $10 \text{ m}^2 \text{ s}^{-1}$ for a typical 50 km radius
522 Meddy. If Meddies and post-convective SCVs have a comparable lifetime T of a few years,
523 the smaller radius L of SCVs would tend to reduce their associated diffusion coefficient
524 ($\propto L^2 T^{-1}$). The physics of the dissipation of Meddies and post-convective SCVs is likely
525 to involve different processes. While the rim of Meddies is a place of intense layering
526 [*Meunier et al.*, 2015] and their core is known to be subjected to double diffusive convection
527 and salt-fingering [*Armi et al.*, 1989], the SCV studied here does not exhibit the typical
528 features associated with those processes (horizontal interleaving or vertical staircases in
529 temperature and salinity).

530 As stated before, *McWilliams* [1985] highlighted the link between the SCV vorticity
531 and its ability to overcome interactions with external flows. Here, the extreme negative
532 vorticity ($-0.8f$) sets important dynamical barriers within the core that drastically inhibit
533 lateral exchanges. The background flow is typically characterized by velocities around
534 10 cm s^{-1} at 500 m depth and horizontal scales of about 10 km , leading to horizontal
535 shear order of $0.1f$. Recently, *Damien et al.* [in revision, this issue] managed to simulate

536 post-convective SCVs of 5 km radius in a realistic high-resolution regional simulation. The
537 SCVs similarly show a slow diffusion of their core properties with an estimated diffusion
538 coefficient of $0.6 \text{ m}^2 \text{ s}^{-1}$ in coherence with our estimates. They could survived many
539 interactions with external flows before being finally dissipated by the convective event
540 occurring the following winter.

3.4. Biogeochemical and biological impacts

541 3.4.1. Impact on nutrients concentration

542 The SCV has an important impact on the nutrients distribution (see figure 8-a,b,c).
543 Close to the surface, all nutriclines seem to be shallower by 20 to 50 m compared to
544 the background environment leading to an enhancement of the nutrient availability at
545 the base of the euphotic layer. Within the SCV core between 300 m and about 1500 m
546 depth, the three main nutrients (Nitrate, Phosphate, Silicate) are significantly depleted
547 with respective concentrations around 700 m of 6.9, 0.34 and $6.6 \mu\text{mol L}^{-1}$. This is a
548 decrease of 18, 13 and 18% compared to background concentrations. As for other tracers,
549 nutrients remain isolated from the surrounding environment because of the very limited
550 lateral exchanges.

551 The formation process of the SCV can provide an explanation for these low values.
552 Indeed, it results from the mixing of nutrients-poor surface waters with richer waters.
553 Schematically, a 100 m thick surface layer with no nutrients being mixed with 700 m
554 of nutrient-rich waters below would result in a nutrient concentration reduced by about
555 13%. Following this argument, among the other type of post-convective SCVs described
556 in *Bosse et al.* [2016], anticyclones with a deep core below 1000 m and cyclones of newly

557 formed deep waters would certainly have a less marked imprint on the nutrients, whereas
558 shallower Winter Intermediate Water SCVs would be even more nutrients-depleted.

559 **3.4.2. Impact on phytoplankton**

560 The radial distribution of chlorophyll-a measured by the glider is shown in figure 9-
561 a. Both $[Chl_a]$ at the deep chlorophyll maximum (DCM) and integrated over the top
562 200 m reveal much higher concentrations inside the eddy with respectively 1.7 mg m^{-3}
563 ($+113\%$) and 29 mg m^{-2} ($+38\%$) (figure 9-b,c). The eddy dynamics seems thus to favor
564 phytoplankton growth, much likely as a result of the isopycnals doming characteristic of
565 cyclonic and "Mode Water" anticyclones [*McGillicuddy et al., 2007; Nencioli et al., 2008*].
566 The isopycnals doming is quite marked at about 100 m deep, while it is dumped closer to
567 the surface due to summer stratification. This can explain why nutriclines are displaced
568 of about 20-50 m increasing the nutrients availability, whereas the DCM only moves by
569 less than 10 m (figure 9-d).

570 Regarding the phytoplankton size group, HPLC measurements show a clear predomi-
571 nance of nanophytoplankton inside the eddy with a concentration of 0.86 mg m^{-3} , about
572 twice the median value of 0.44 mg m^{-3} observed in the Ligurian Sea (see figure 9-e). This
573 is one of the most abundant station for nanophytoplankton, which represents almost 80%
574 of the total chlorophyll-a. Note that the glider fluorometer calibrated with satellite images
575 is in good agreement with the total chlorophyll-a concentration of 1.1 mg m^{-3} measured
576 by HPLC.

4. Discussion

4.1. Fate and decline of post-convective SCVs

577 Deep SCVs are among the most coherent circulation features in the ocean and represent
578 local oddities for the diffusion of tracers. For the diffusive cylinder, the tracer concen-
579 tration will reach half of its initial value after $L^2/0.20K_\rho$. Given the diffusion coefficient
580 estimated here, it yields a typical lifetime of 28 months. The SCVs here observed 4.5
581 months after its formation can be considered as still being in its early stage of life. This
582 is new evidence of the extended lifetime of SCVs already observed [*Testor and Gascard,*
583 2003; *Budéus et al., 2004; Testor and Gascard, 2006; Bosse et al., 2016*].

584 For long, it has been considered that lateral intrusions driven by double-diffusion are
585 causing the decay of Meddies. However, new theories on the origin of those intrusions were
586 recently made implying flow instability and stirring processes [*Hua et al., 2013; Meunier*
587 *et al., 2015*]. Here, it is hard to see any intrusion at the rim of the SCV, the gradients
588 separating the SCV and the surroundings being pretty sharp for each eddy crossing by
589 the glider (see figure 2-c). Anticyclonic eddies can also trap downward propagating near-
590 inertial waves, as it has already been observed [*Joyce et al., 2009; Cuypers et al., 2012;*
591 *Sheen et al., 2015; Karstensen et al., in review, 2016*]. The energy dissipation of those
592 waves and their influence on the decay of small-scale post-convective SCVs would need to
593 be assessed in future studies with help of complementary turbulence measurements and
594 numerical models.

4.2. Deep mixing preconditioning

595 As SCVs can live for an extended period of time and are very resistant to interactions,
596 they can easily survive until the following winter. Vertical mixing is actually a primary

597 generation mechanism of SCVs, but plays also likely an important role in their dissipa-
598 tion. Due to the deformation of isopycnal layers associated with them, they also have an
599 influence on the deepening of the mixed layer [Legg *et al.*, 1998; Lherminier *et al.*, 1999;
600 Bosse *et al.*, 2015, 2016]. For an anticyclonic SCV, once the vertical mixing reaches the
601 top of its weakly stratified core, it then requires a lot less buoyancy loss to mix it down
602 to the base of the core.

603 The heat and salt content anomalies integrated between the center and one eddy radius
604 represent respectively $+4.0 \times 10^9$ kg of salt and $+4.7 \times 10^{16}$ J. This values are comparable to
605 what was found for LIW SCVs by Bosse *et al.* [2015]. This suggests that post-convective
606 SCVs of Winter Deep Waters can have an equally important role in the vertical and
607 horizontal heat/salt transport across the NW Mediterranean. The large amount of heat
608 and salt they transport can eventually be redistributed within the mixed layer, thus
609 impacting the heat/salt budget of the deep waters, as discussed by Bosse *et al.* [2015] for
610 LIW SCVs.

4.3. Surface signature of a subsurface SCV

611 The detection of subsurface eddies from space is an active research topic (see [Klemas
612 and Yan, 2014] for a review). However, in weakly stratified oceans like the Mediterranean
613 Sea characterized by a small deformation radius, gridded altimetry products have a too
614 large decorrelation scale compared to the observed oceanic variability associated with
615 SCVs and standalone along-track measurements that could tentatively resolve them are
616 hard to interpret. In this context, ocean color images can be very useful, as they provide
617 insights at very high resolution (1 km) into the surface dynamics at the only condition
618 that the sky remains cloud-free. Sea surface temperature measured by satellite at high

619 resolution have also been examined. The figure 4-a indeed suggests that surface waters
620 are 0.1–0.2°C colder inside the eddy. However, the summertime heating of the superficial
621 layers very likely prevents such a signal to be captured.

622 Figure 10 shows the evolution of the surface chlorophyll-a concentration seen by satellite.
623 It reveals a clear clockwise swirling of a chlorophyll patch around the outer edge of the
624 deep SCV. Despite lower velocities of about 5 cm s^{-1} , the SCV seems however to act on
625 the surface dynamics (see figure 5-a). Like at great depths, dynamical barriers similarly
626 prevent lateral exchanges between the eddy core and the surroundings. Generally, the
627 surface chlorophyll signal associated with subsurface post-convective SCVs would then be
628 sensitive to the context of its surrounding environment, unlike its subsurface signature
629 characterized by an enhanced deep chlorophyll maximum.

4.4. Primary production and carbon sequestration

630 The primary production is estimated from HPLC measurements by applying a bio-
631 optical model [Morel, 1991]. It shows an important influence of the SCV compared to other
632 stations carried out in the Ligurian Sea (see figure 9-f). The total primary production
633 reaches $0.76 \text{ gC m}^{-2} \text{ d}^{-1}$ about 25% more than the average value in the Ligurian Sea
634 ($0.6 \text{ gC m}^{-2} \text{ d}^{-1}$). The contribution of the different phytoplankton size groups to this
635 elevated primary production again reveals the importance of nanophytoplankton. This
636 can have further implication for the carbon sequestration, as higher productivity also
637 means enhanced export of particulate organic carbon to great depths where it can be
638 remineralized under the action of bacteria. Higher carbon export within mesoscale eddies
639 was already reported in Mediterranean Sea by *Moutin and Prieur* [2012]. *Waite et al.*
640 [2016] recently described an important mechanism that concentrates particulate export

641 within mesoscale eddies. The remineralization would imply a gradual increase in the
642 nutrients concentration. The SCV's core however remained nutrients-depleted even after
643 more than 4 months of remineralization.

644 Dissolved inorganic carbon measurements also reveals a higher concentration within
645 the SCV of about 5–10 $\mu\text{mol kg}^{-1}$. As discussed before, this could result from the higher
646 productivity associated with it. Another explanation could be the trapping at depth of
647 organic carbon during wintertime, while the SCV is formed. Indeed, figure 1-c shows a
648 clear signal of chlorophyll-a below the euphotic layer within the mixed layer and down to
649 1000 m. Phytoplankton cells initially present in the surface layer are then diluted over the
650 mixed layer during active mixing characterized by intense vertical water displacements of
651 $\pm 5\text{--}15 \text{ cm s}^{-1}$ [Schott and Leaman, 1991; Marshall and Schott, 1999; Margirier et al.,
652 submitted, this issue]. This allows within a few hours the overturning of phytoplankton
653 between the euphotic layer and depths of about 1000 m. During the generation of post-
654 convective SCV, vertical motions cease and phytoplankton would get trapped within the
655 deep core before being converted into inorganic carbon.

5. Summary and Conclusion

656 This study described the dynamical and biogeochemical characteristics of a Subme-
657 soscale Coherent Vortex (SCV) formed by deep convection in the Ligurian Sea (NW
658 Mediterranean Sea). It is based on *in situ* observations collected in late June 2013 during
659 a research cruise (shipborne CTD measurements and water samples analysis) combined
660 with data from an autonomous glider equipped with optode and bio-optical sensors. It
661 was very fortunate that the glider crossed the eddy a few days after the ship, but the
662 opportunity was taken to intensively sample the eddy with the glider.

663 Its core is made of nearly homogeneous water between 300 and 1200 m depth with
664 $\theta \simeq 13.18^\circ\text{C}$, $S_P \simeq 38.54$ and $\text{DO} \simeq 200 \mu\text{mol kg}^{-1}$. The high dissolved oxygen concen-
665 tration of the SCV indicates an origin during the previous wintertime convective episode
666 about 4.5 month prior to its sampling during summer. The presence of very warm and
667 salty Levantine Intermediate Waters around it suggests it has been interacting with the
668 boundary circulation flowing along the continental slope along Sardinia and Corsica.

669 The SCV has an intense anticyclonic rotation with depth-average currents measured
670 by the glider up to 15 cm s^{-1} . Those currents were used to detect the eddy center and
671 reconstruct the fine-scale eddy dynamics. The equilibrium depth of the SCV is around
672 700 m, where cyclogeostrophic peak velocities of 13.9 cm s^{-1} are estimated at a distance
673 of 6.2 km from the center. The force balance of the eddy is found to be strongly non
674 linear with a Rossby number at the velocity maximum of -0.45 . The shear at the origin
675 is even higher and reaches $-0.8f$. This suggests a great ability of the SCV to overcome
676 the interaction with external flows. The Burger number of the SCV is close to unity
677 indicating a high aspect ratio of this circulation feature. The vertical stratification N is
678 reduced within the core with a mean core stratification of about $2.4f$. Due to this low value
679 and to the high anticyclonic vorticity, the potential vorticity of the SCV reaches values
680 as low as $10^{-13} \text{ m}^{-1} \text{ s}^{-1}$ testifying to the strong mixing occurring during its generation.

681 The extensive sampling of the eddy core and the knowledge of the age of the eddy enable
682 to estimate a lateral isopycnic coefficient by solving the cylindrical diffusion equation. It
683 yields a diffusive coefficient of $0.22 \text{ m}^2 \text{ s}^{-1}$. The diffusive half-life of the eddy is thus of
684 about 2.5 years. So, even after 4.5 months of existence, the SCV can still be considered
685 as being in its early stage of life. Important dynamical barriers drastically reduce lateral

686 exchanges between the core of the SCV and the surroundings thus enabling it to keep the
687 characteristics of its origin (i.e. ventilated waters with almost constant temperature and
688 salinity). Furthermore, it has the ability to easily survive until the following winter. As
689 interactions with other flows and diffusive processes have little impact on the SCV, winter
690 vertical mixing is likely to be an important mechanism for the destruction of such very
691 coherent SCVs. In the future, the utilization of turbulence sensors mounted on gliders
692 could unveil the mysteries about the SCVs fate and in particular their interaction with
693 internal waves.

694 In terms of biogeochemical properties, the SCV core is nutrient-depleted with concen-
695 trations in nitrate, phosphate and silicate on average -15% lower than what is found in
696 the surroundings at about 700 m. Nutriclines are shifted toward the surface by about 20–
697 50 m, enhancing the nutrients availability for phytoplankton growth. Consistently, the
698 glider fluorometer and HPLC measurements reveal higher chlorophyll-a concentrations
699 of the deep chlorophyll maximum within the eddy (1.7 mg m^{-3} , $+90\%$). Furthermore,
700 pigments concentrations show a clear predominance of nanophytoplankton compared to
701 outside. This demonstrates that even deep SCVs have a significant influence on the nutri-
702 ents distribution and the phytoplankton community. A bio-optical model was also used
703 to characterized the primary production. It was found to be significantly enhanced inside
704 the SCV leading potentially to a higher carbon sequestration.

705 This study gives the first conjoint physic-biogeochemical description of a post-convective
706 SCV in the NW Mediterranean Sea. Our findings suggest they locally have a great
707 imprint on both physical and biogeochemical cycles. However, their basin-scale impact
708 in particular for the nutrients budget or the phytoplankton distribution still need to be

709 assessed. This is an important issue for coupled regional climate model that do not resolve
 710 those processes, but still aim at characterizing the evolution of the marine ecosystem in
 711 the context of climate change.

Appendix A: The heat equation in cylindrical coordinate

Lets consider the evolution of a tracer T whose concentration is initially constant $T = T_0$ and confined within a long cylinder of radius R . In this case, the heat equation goes by in its cylindrical form:

$$\frac{\partial T}{\partial t} = K \frac{1}{r} \frac{\partial}{\partial r} \left(r \frac{\partial T}{\partial r} \right) \quad (\text{A1})$$

712 The desired solution of this equation owes to verify: (1) $\partial_r T = 0$ at $r = 0$ as imposed
 713 by the cylindrical geometry; (2) $T = T_\infty$ at $r = L$ as the background domain is supposed
 714 to be infinite and thus have a constant tracer concentration.

715 According to the separation of variables method, we can seek a solution of the form:
 716 $T(r, t) = T_\infty + \alpha(r)\beta(t)$. Substituting this into the heat equation yields:

$$\frac{1}{r\alpha} \frac{d}{dr} \left(r \frac{d\alpha}{dr} \right) = \frac{1}{K} \frac{1}{\beta} \frac{d\beta}{dt} \quad (\text{A2})$$

Each side of the equation being a function of an independent variable (r and t), it has thus to be constant. Furthermore, this constant must be negative to prevent β from exponentially diverging in time. Lets call it $-\lambda^2$, we then have:

$$r^2 \frac{d^2 \alpha}{dr^2} + r \frac{d\alpha}{dr} + r^2 \lambda^2 = 0 \quad \text{and} \quad \frac{d\beta}{dt} + K \lambda^2 \beta = 0 \quad (\text{A3})$$

717 The general solution for β is simply: $\beta(t) = \beta_0 e^{-\lambda^2 D t}$ where β_0 is a constant.

718 The equation on α is a special case of Bessel's equation, whose only physically mean-
 719 ingful solution has the form: $\alpha(r) = \alpha_0 J_0(\lambda r)$ where α_0 is another constant and J_0 is the
 720 Bessel function of first kind of order zero.

Since $T(r = L, t) = T_\infty$, this requires $J_0(\lambda L) = 0$. Knowing the zeros of the Bessel function J_0 , one can thus define λ_n the eigenvalues of the problem and the particular solutions for the problem: $T_n(r, t) = T_\infty + A_n J_0(\lambda_n r) e^{-\lambda_n^2 D t}$ with $A_n = \alpha_0^n \beta_0$. The general solution then writes:

$$T(r, t) = T_\infty + \sum_{n=1}^{\infty} A_n J_0(\lambda_n r) e^{-\lambda_n^2 K t} \quad (\text{A4})$$

To infer the coefficients A_n , one can project the initial condition ($T(r, t = 0) - T_\infty = T_0 - T_\infty$) onto a particular eigenfunction $J_0(\lambda_m r)$ and use the orthogonality of each eigenfunction ($\int_{[0,L]} r J_0(\lambda_m r) J_0(\lambda_n r) dr = 0$ if $n \neq m$, $= 1$ otherwise):

$$\int_0^L r J_0(\lambda_m r) (T_0 - T_\infty) dr = \sum_{n=1}^{\infty} \int_0^L r A_n J_0(\lambda_m r) J_0(\lambda_n r) dr = A_m \int_0^L r J_0(\lambda_m r)^2 dr \quad (\text{A5})$$

then knowing that: $\int_{[0,L]} r J_0(\lambda_m r) dr = L J_1(\lambda_m L) / \lambda_m$ and $\int_{[0,L]} r J_0^2(\lambda_m r) dr = L^2 [J_0^2(\lambda_m L) + J_1^2(\lambda_m L)] / 2 = L^2 J_1^2(\lambda_m L) / 2$, one can explicit the different coefficient A_m and write the final solution of our problem:

$$T(r, t) = T_\infty + \frac{2(T_0 - T_\infty)}{L} \sum_{n=1}^{\infty} \frac{J_0(\lambda_n r)}{\lambda_n J_1(\lambda_n L)} e^{-\lambda_n^2 K t} \quad (\text{A6})$$

721 Acknowledgments.

722 The hydrographical data were collected and made freely available by the Coriolis project
 723 and programmes that contribute to it (<http://www.coriolis.eu.org>). The cruise data is
 724 provided in the reference section along with the associated doi. Vincent Tailliandier is
 725 thanked for the calibration of shipborne CTD and providing feedback on the manuscript.
 726 We would like to acknowledge the staff of the French National Pool of Gliders of DT-INSU

727 (CNRS/Ifremer) for the sustained gliders deployments carried out in the framework of
728 MOOSE, as well as the intensive deployments during this 2012–2013 DEWEX experi-
729 ment. Captains and crew of R/V *Le Tethys II* (CNRS/INSU) and *Le Suroit* (Ifremer)
730 as well as all scientists, engineers and technicians who participated to the MOOSE-GE
731 and DEWEX different cruises and autonomous platforms deployments are also warmly
732 thanked. Support was provided by the French the French "Chantier Méditerranée" MIS-
733 TRALS program (HyMeX and MERMeX components) and the French MOOSE long-term
734 observatory (SOERE/AllEnvi-SNO/INSU), as well as by th EU projects FP7 GROOM
735 (Grant Agreement No. 284321), FP7 PERSEUS (Grant Agreement No. 287600) and FP7
736 JERICO (Grant Agreement No. 262584) and the COST Action ES0904 "EGO" (Every-
737 one's Gliding Observatories). A. Bosse was funded by a French government scholarship.

References

- 738 Aminot, A., and R. K erouel, *Dosage automatique des nutriments dans les eaux marines*,
739 Ed. Ifremer, 2007.
- 740 Armi, L., D. Hebert, N. Oakey, J. F. Price, P. L. Richardson, H. T. Rossby, and B. Rud-
741 dick, Two Years in the Life of a Mediterranean Salt Lens, *Journal of Physical Oceanog-*
742 *raphy*, 19, 354–370, 1989.
- 743 B ethoux, J.-P., B. Gentili, J. Raunet, and D. Tailliez, Warming trend in the western
744 Mediterranean deep water, *Nature*, 347, 660–662, 1990.
- 745 Bosse, A., Circulation g en erale et couplage physique-biog eochimie   (sous-)m eso echelle
746 en M editerran ee Nord-occidentale   partir de donn ees in situ, Ph.D. thesis, Universit e
747 Pierre et Marie Curie, Paris, 2015.

- 748 Bosse, A., P. Testor, L. Mortier, L. Prieur, V. Taillandier, F. D’Ortenzio, and L. Cop-
749 pola, Spreading of Levantine Intermediate Waters by submesoscale coherent vortices in
750 the northwestern Mediterranean Sea as observed with gliders, *Journal of Geophysical*
751 *Research: Oceans*, *120*, 1599–1622, 2015.
- 752 Bosse, A., et al., Scales and dynamics of submesoscale coherent vortices formed by deep
753 convection in the northwestern mediterranean sea, *Journal of Geophysical Research:*
754 *Oceans*, *121*, 7716–7742, 2016.
- 755 Bouffard, J., A. Pascual, S. Ruiz, Y. Faugère, and J. Tintoré, Coastal and mesoscale
756 dynamics characterization using altimetry and gliders: A case study in the Balearic
757 Sea, *Journal of Geophysical Research: Oceans*, *115*, 1–17, 2010.
- 758 Bouffard, J., L. Renault, S. Ruiz, A. Pascual, C. Dufau, and J. Tintoré, Sub-surface
759 small-scale eddy dynamics from multi-sensor observations and modeling, *Progress in*
760 *Oceanography*, *106*, 62–79, 2012.
- 761 Bower, A. S., R. M. Hendry, D. E. Amrhein, and J. M. Lilly, Direct observations of
762 formation and propagation of subpolar eddies into the subtropical North Atlantic, *Deep*
763 *Sea Res. II*, *85*, 15–41, 2013.
- 764 Bretherton, F. P., R. E. Davis, and C. B. Fandry, A technique for objective analysis
765 and design of oceanographic experiments applied to MODE-73, *Deep Sea Research and*
766 *Oceanographic Abstracts*, *23*, 559–582, 1976.
- 767 Budéus, G., B. Cisewski, S. Ronski, D. Dietrich, and M. Weitere, Structure and effects of
768 a long lived vortex in the Greenland Sea, *Geophysical Research Letters*, *31*, 1–5, 2004.
- 769 Carpenter, J. R., and M.-L. Timmermans, Deep mesoscale eddies in the Canada Basin,
770 Arctic Ocean, *Geophysical Research Letters*, *39*, 1–6, 2012.

- 771 Ciani, D., X. Carton, I. Bashmachnikov, B. Chapron, and X. Perrot, Influence of Deep
772 Vortices on the Ocean Surface, *Discontinuity, Nonlinearity, and Complexity*, 4, 281–
773 311, 2015.
- 774 Claustre, H., The trophic status of various oceanic provinces as revealed by phytoplankton
775 pigment signatures, *Limnology and Oceanography*, 39, 1206–1210, 1994.
- 776 Cotroneo, Y., G. Aulicino, S. Ruiz, A. Pascual, G. Budillon, G. Fusco, and J. Tintoré,
777 Glider and satellite high resolution monitoring of a mesoscale eddy in the algerian basin:
778 Effects on the mixed layer depth and biochemistry, *Journal of Marine Systems*, 2015.
- 779 Cuypers, Y., P. Bouruet-Aubertot, C. Marec, and J.-L. Fuda, Characterization of tur-
780 bulence from a fine-scale parameterization and microstructure measurements in the
781 Mediterranean Sea during the BOUM experiment, *Biogeosciences*, 9, 3131–3149, 2012.
- 782 Damien, P., A. Bosse, P. Testor, P. Marsaleix, and C. Estournel, Modelling post convec-
783 tive submesoscale coherent vortices in the mediterranean sea, *Journal of Geophysical*
784 *Research: Oceans*, in revision, this issue.
- 785 D’Asaro, E., Observations of small eddies in the Beaufort Sea, *Journal of Geophysical*
786 *Research*, 93, 6669–6684, 1988.
- 787 DOE, *Handbook of Methods for the Analysis of the Various Parameters of the Car-*
788 *bon Dioxide System in Sea Water; version 2*, A. G. Dickson and C. Goyet, eds.,
789 ORNL/CDIAC-74, 1994.
- 790 Durrieu de Madron, X., et al., Marine ecosystems’ responses to climatic and anthropogenic
791 forcings in the Mediterranean, *Progress in Oceanography*, 91, 97–166, 2011.
- 792 Durrieu de Madron, X., et al., Deep sediment resuspension and thick nepheloid layer
793 generation by open-ocean convection, *Journal of Geophysical Research: Oceans*, pp.

- 794 n/a–n/a, 2017.
- 795 Elliott, B. A., and T. B. Sanford, The Subthermocline Lens D1. Part II: Kinematics and
796 Dynamics, *Journal of Physical Oceanography*, *16*, 549–561, 1986.
- 797 Ertel, H., Ein neuer hydrodynamischer wirbelsatz, *Meteorol. Z.*, *59*, 277–281, 1942.
- 798 Estournel, C., et al., HyMeX-SOP2, the field campaign dedicated to dense water formation
799 in the north-western Mediterranean, *Oceanography*, accepted.
- 800 Fan, X., U. Send, P. Testor, J. Karstensen, P. Lherminier, and G. Drive, Observations
801 of Irminger Sea Anticyclonic Eddies, *Journal of Physical Oceanography*, *43*, 805–823,
802 2013.
- 803 Frajka-Williams, E., P. B. Rhines, and C. C. Eriksen, Physical controls and mesoscale
804 variability in the Labrador Sea spring phytoplankton bloom observed by Seaglider,
805 *Deep Sea Research Part I: Oceanographic Research Papers*, *56*, 2144–2161, 2009.
- 806 Garau, B., S. Ruiz, W. G. Zhang, A. Pascual, E. E. Heslop, J. Kerfoot, and J. Tintoré,
807 Thermal Lag Correction on Slocum CTD Glider Data, *Journal of Atmospheric and
808 Oceanic Technology*, *28*, 1065–1071, 2011.
- 809 Gascard, J.-C., Mediterranean deep water formation baroclinic instability and oceanic
810 eddies, *Oceanologica Acta*, *1*, 315–330, 1978.
- 811 Gascard, J.-c., A. J. Watson, M.-J. Messias, K. A. Olsson, T. Johannessen, and K. Simon-
812 sen, Long-lived vortices as a mode of deep ventilation in the Greenland Sea, *Nature*,
813 *416*, 525–527, 2002.
- 814 Gasparini, G. P., A. Ortona, G. Budillon, M. Astraldi, and E. Sansone, The effect of the
815 Eastern Mediterranean Transient on the hydrographic characteristics in the Strait of
816 Sicily and in the Tyrrhenian Sea, *Deep-Sea Research Part I: Oceanographic Research*

- 817 *Papers*, 52, 915–935, 2005.
- 818 Hebert, D., N. Oakey, and B. Ruddick, Evolution of a Mediterranean Salt Lens: Scalar
819 Properties, *Journal of Physical Oceanography*, 20, 1468–1483, 1990.
- 820 Houpert, L., et al., Observations of open-ocean deep convection in the northwestern
821 mediterranean sea: Seasonal and interannual variability of mixing and deep water
822 masses for the 20072013 period, *Journal of Geophysical Research: Oceans*, pp. n/a–
823 n/a, 2016.
- 824 Hua, B. L., C. Ménesguen, S. Le Gentil, R. Schopp, B. Marsset, and H. Aiki, Layering
825 and turbulence surrounding an anticyclonic oceanic vortex: in situ observations and
826 quasi-geostrophic numerical simulations, *Journal of Fluid Mechanics*, 731, 418–442,
827 2013.
- 828 Janzen, C., D. Murphy, and N. Larson, Getting more mileage out of dissolved oxygen
829 sensors in long-term moored applications, in *OCEANS 2007*, pp. 1–5, 2007.
- 830 Jones, H., and J. Marshall, Restratification after Deep Convection, *Journal of Physical*
831 *Oceanography*, 27, 2276–2287, 1997.
- 832 Joyce, T. M., L. N. Thomas, and F. Bahr, Wintertime observations of Subtropical Mode
833 Water formation within the Gulf Stream, *Geophysical Research Letters*, 36, 1–5, 2009.
- 834 Juza, M., L. Renault, S. Ruiz, and J. Tintoré, Origin and pathways of Winter Intermediate
835 Water in the Northwestern Mediterranean Sea using, *J. Geophys. Res.*, 2013.
- 836 Karstensen, J., et al., Upwelling and isolation in oxygen-depleted anticyclonic modewater
837 eddies and implications for nitrate cycling, *Biogeosciences Discussions*, pp. 1–25, in
838 review, 2016.

- 839 Kirkwood, D. S., Stability of solutions of nutrient salts during storage, *Marine Chemistry*,
840 38, 151–164, 1992.
- 841 Klemas, V., and X. H. Yan, Subsurface and deeper ocean remote sensing from satellites:
842 An overview and new results, *122*, 1–9, 2014.
- 843 Kloosterziel, R. C., G. F. Carnevale, and P. Orlandi, Inertial instability in rotating and
844 stratified fluids: barotropic vortices, *Journal of Fluid Mechanics*, 583, 379–412, 2007.
- 845 Krahnemann, G., and F. Schott, Longterm increases in western Mediterranean salinities
846 and temperatures: Anthropogenic and climatic sources, *Geophysical Research Letters*,
847 25, 4209, 1998.
- 848 Kunze, E., R. W. Schmitt, and J. M. Toole, The energy balance in a warm-core ring’s
849 near-inertial critical layer, *Journal of Physical Oceanography*, 25, 942–957, 1995.
- 850 Lachkar, Z., S. Smith, M. Levy, and O. Pauluis, Eddies reduce denitrification and compress
851 habitats in the Arabian Sea, *Geophysical Research Letters*, 2016.
- 852 Lavigne, H., F. D’Ortenzio, H. Claustre, and A. Poteau, Towards a merged satellite and
853 in situ fluorescence ocean chlorophyll product, *Biogeosciences*, 9, 2111–2125, 2012.
- 854 Le Traon, P.-Y., IOpt, *Journal of Geophysical Research*, 95, 543–547, 1990.
- 855 Leaman, K. D., and F. a. Schott, Hydrographic Structure of the Convection Regime in
856 the Gulf of Lions: Winter 1987, *Journal of Physical Oceanography*, 21, 575–598, 1991.
- 857 Legg, S., and J. C. Marshall, A Heton Model of the Spreading Phase of Open-Ocean Deep
858 Convection, *Journal of Physical Oceanography*, 23, 1040–1056, 1993.
- 859 Legg, S., J. McWilliams, and J. Gao, Localization of Deep Ocean Convection by a
860 Mesoscale Eddy, *Journal of Physical Oceanography*, 28, 944–970, 1998.

- 861 Lherminier, P., J.-C. Gascard, and D. Quadfasel, The Greenland Sea in Water 1993 and
862 1994: preconditioning for deep convection, *Deep Sea Research Part II: Topical Studies*
863 *in Oceanography*, *46*, 1199–1235, 1999.
- 864 Lilly, J. M., and P. B. Rhines, Coherent Eddies in the Labrador Sea Observed from a
865 Mooring, *Journal of Physical Oceanography*, *32*, 585–598, 2002.
- 866 Löscher, C. R., et al., Hidden biosphere in an oxygen-deficient Atlantic open-ocean eddy:
867 Future implications of ocean deoxygenation on primary production in the eastern trop-
868 ical North Atlantic, *Biogeosciences*, *12*, 7482—7482, 2015.
- 869 Margirier, F., A. Bosse, P. Testor, B. L’Hévéder, L. Mortier, and D. Smeed, Characteriza-
870 tion of convective plumes associated with oceanic deep convection in the Northwestern
871 Mediterranean from high resolution in-situ data collected by gliders, *Journal of Geo-*
872 *physical Research*, submitted, this issue.
- 873 Marshall, J., and F. Schott, Open-ocean convection: Observations, theory, and models,
874 *Reviews of Geophysics*, *37*, 1–64, 1999.
- 875 Martin, J. P., C. M. Lee, C. C. Eriksen, C. Ladd, and N. B. Kachel, Glider observations
876 of kinematics in a Gulf of Alaska eddy, *Journal of Geophysical Research*, *114*, 1–19,
877 2009.
- 878 Mayot, N., F. d’Ortenzio, V. Taillandier, L. Prieur, O. P. de Fommervault, H. Claustre,
879 A. Bosse, P. Testor, and P. Conan, Impacts of the deep convection on the phytoplankton
880 blooms in temperate seas: a multiplatform approach over a complete annual cycle (2012-
881 2013 DEWEX experiment), *Journal of Geophysical Research*, in revision, this issue.
- 882 Mayot, N., F. d’Ortenzio, J. Uitz, B. Gentili, J. Ras, V. Vellucci, M. Golbol, D. Antoine,
883 and H. Claustre, Influence of the phytoplankton community structure on the spring

- 884 and annual primary production in the North-Western Mediterranean Sea, *Journal of*
885 *Geophysical Research*, submitted, this issue.
- 886 McGillicuddy, D. J., et al., Eddy/wind interactions stimulate extraordinary mid-ocean
887 plankton blooms., *Science*, *316*, 1021–6, 2007.
- 888 McWilliams, J. C., Submesoscale, coherent vortices in the ocean, *Reviews of Geophysics*,
889 *23*, 165, 1985.
- 890 McWilliams, J. C., Vortex Generation Through Balanced Adjustment, *Journal of Physical*
891 *Oceanography*, *18*, 1178–1192, 1988.
- 892 McWilliams, J. C., Submesoscale currents in the ocean, *Proceedings of the Royal Society*
893 *of London A: Mathematical, Physical and Engineering Sciences*, *472*, 2016.
- 894 MEDOC-Group, T., Observation of Formation of Deep Water in the Mediterranean Sea,
895 1969, *Nature*, *225*, 1037–1040, 1970.
- 896 Meunier, T., C. Ménesguen, R. Schopp, and S. Le Gentil, Tracer Stirring around a Meddy:
897 The Formation of Layering, *Journal of Physical Oceanography*, *45*, 407–423, 2015.
- 898 Millot, C., The circulation of the Levantine Intermediate Water in the Algerian Basin,
899 *Journal of Geophysical Research*, *92*, 8265, 1987.
- 900 Millot, C., Circulation in the Western Mediterranean Sea, *J. Mar. Syst.*, *20*, 423–442,
901 1999.
- 902 Morel, A., Light and marine photosynthesis: a spectral model with geochemical and
903 climatological implications, *Progress in Oceanography*, *1991*, 263 – 306, 1991.
- 904 Morel, A., and J.-F. Berthon, Surface pigments, algal biomass profiles, and potential
905 production of the euphotic layer: Relationships reinvestigated in view of remote-sensing
906 applications, *Limnology and Oceanography*, *34*, 1545–1562, 1989.

- 907 Morel, A., and S. Maritorena, Bio-optical properties of oceanic waters: A reappraisal,
908 *Journal of Geophysical Research: Oceans*, *106*, 7163–7180, 2001.
- 909 Moutin, T., and L. Prieur, Influence of anticyclonic eddies on the Biogeochemistry
910 from the Oligotrophic to the Ultraoligotrophic Mediterranean (BOUM cruise), *Bio-*
911 *geosciences*, *9*, 3827–3855, 2012.
- 912 Nencioli, F., V. S. Kuwahara, T. D. Dickey, Y. M. Rii, and R. R. Bidigare, Physical
913 dynamics and biological implications of a mesoscale eddy in the lee of Hawai'i: Cyclone
914 Opal observations during E-Flux III, *Deep-Sea Research Part II: Topical Studies in*
915 *Oceanography*, *55*, 1252–1274, 2008.
- 916 Nencioli, F., F. d'Ovidio, A. M. Doglioli, and A. A. Petrenko, In situ estimates of sub-
917 mesoscale horizontal eddy diffusivity across an ocean front, *Journal of Geophysical Re-*
918 *search: Oceans*, *118*, 7066–7080, 2013.
- 919 Okubo, A., Oceanic diffusion diagrams, *Deep Sea Research and Oceanographic Abstracts*,
920 *18*, 789–802, 1971.
- 921 Pelland, N. A., C. C. Eriksen, and C. M. Lee, Subthermocline Eddies over the Washington
922 Continental Slope as Observed by Seagliders, 2003-09, *Journal of Physical Oceanogra-*
923 *phy*, *43*, 2025–2053, 2013.
- 924 Penven, P., I. Halo, S. Pous, and L. Marie, Cyclogeostrophic balance in the Mozambique
925 Channel, *Journal of Geophysical Research: Oceans*, *119*, 1054–1067, 2014.
- 926 Pingree, R. D., and B. Le Cann, A shallow meddy (a smeddy) from the secondary Mediter-
927 ranean salinity maximum, *Journal of Geophysical Research*, *98*, 169–185, 1993.
- 928 Prater, M. D., and T. B. Sanford, A Meddy Off Cape-St-Vincent .1. Description, *Journal*
929 *of Physical Oceanography*, *24*, 1572–1586, 1994.

- 930 Provenzale, A., Transport by coherent barotropic vortices, *Annual Review of Fluid Me-*
931 *chanics*, *31*, 55–93, 1999.
- 932 Ras, J., H. Claustre, and J. Uitz, Spatial variability of phytoplankton pigment distribu-
933 tions in the subtropical south pacific ocean: comparison between in situ and predicted
934 data, *Biogeosciences*, *5*, 353–369, 2008.
- 935 Rhines, P. B., and W. R. Young, How rapidly is a passive scalar mixed within closed
936 streamlines?, *Journal of Fluid Mechanics*, *133*, 133–145, 1983.
- 937 Schott, F., and K. D. Leaman, Observations with Moored Acoustic Doppler Current
938 Profilers in the Convection Regime in the Golfe du Lion, 1991.
- 939 Schroeder, K., J. Chiggiato, H. L. Bryden, M. Borghini, and S. Ben Ismail, Abrupt climate
940 shift in the Western Mediterranean Sea, *Scientific Reports*, *6*, 23,009, 2016.
- 941 Send, U., J. Font, and C. Mertens, Recent observation indicates convection’s role in deep
942 water circulation, *Eos*, *77*, 61–65, 1996.
- 943 Sheen, K. L., J. A. Brearley, A. C. Naveira Garabato, D. A. Smeed, L. S. Laurent, M. P.
944 Meredith, A. M. Thurnherr, and S. N. Waterman, Modification of turbulent dissipation
945 rates by a deep southern ocean eddy, *Geophysical Research Letters*, *42*, 3450–3457,
946 2015, 2015GL063216.
- 947 Somot, S., F. Sevault, and M. Déqué, Transient climate change scenario simulation of the
948 Mediterranean Sea for the twenty-first century using a high-resolution ocean circulation
949 model, *Climate Dynamics*, *27*, 851–879, 2006.
- 950 Testor, P., DEWEX-MERMEX 2013 LEG1 cruise, RV Le Suroît, *Tech. rep.*, 2013.
- 951 Testor, P., and J.-C. Gascard, Large-Scale Spreading of Deep Waters in the Western
952 Mediterranean Sea by Submesoscale Coherent Eddies, *Journal of Physical Oceanogra-*

- 953 *phy*, 33, 75–87, 2003.
- 954 Testor, P., and J.-C. C. Gascard, Post-convection spreading phase in the Northwestern
955 Mediterranean Sea, *Deep Sea Research Part I*, 53, 869–893, 2006.
- 956 Testor, P., L. Coppola, and L. Mortier, MOOSE-GE 2013 cruise, RV Téthys II, *Tech.*
957 *rep.*, 2013.
- 958 Testor, P., et al., Gliders as a component of future observing systems, *Proceedings of*
959 *OceanObs'09: Sustained Ocean Observations and Information for Society (Vol. 2)*,
960 *Venice, Italy, 21-25 September 2009*, J. Hall, D.E. Harrison & D. Stammer Eds., 2010.
- 961 Testor, P., et al., Observation of deep convection in the northwestern Mediterranean sea
962 during winter 2012–2013, *Journal of Geophysical Research: Oceans*, in revision, this
963 issue.
- 964 Thierry, V., and H. Bittig, Argo quality control manual for dissolved oxygen concentration,
965 Argo-BGC Team report, *Tech. rep.*, 2016.
- 966 Thomsen, S., T. Kanzow, G. Krahnemann, R. J. Greatbatch, M. Dengler, and G. Lavik,
967 The formation of a subsurface anticyclonic eddy in the peru-chile undercurrent and
968 its impact on the near-coastal salinity, oxygen, and nutrient distributions, *Journal of*
969 *Geophysical Research: Oceans*, 121, 476–501, 2016.
- 970 Timmermans, M.-L., J. Toole, R. Krishfield, and P. Winsor, Ice-Tethered Profiler obser-
971 vations of the double-diffusive staircase in the Canada Basin thermocline, *Journal of*
972 *Geophysical Research*, 113, 2008.
- 973 Uitz, J., H. Claustre, A. Morel, and S. B. Hooker, Vertical distribution of phytoplankton
974 communities in open ocean: An assessment based on surface chlorophyll, *Journal of*
975 *Geophysical Research: Oceans*, 111, n/a–n/a, 2006, c08005.

- 976 Uitz, J. U., Y. Huot, F. Bruyant, M. Babin, and H. Claustre, Relating phytoplankton
977 photophysiological properties to community structure on large scales, *Limnology and*
978 *Oceanography*, *53*, 614–630, 2008.
- 979 Vargas-Yáñez, M., et al., Extreme Western Intermediate Water formation in winter 2010,
980 *Journal of Marine Systems*, *105-108*, 52–59, 2012.
- 981 Vidussi, F., H. Claustre, B. B. Manca, A. Luchetta, and J.-C. Marty, Phytoplankton pig-
982 ment distribution in relation to upper thermocline circulation in the eastern mediter-
983 ranean sea during winter, *Journal of Geophysical Research: Oceans*, *106*, 19,939–19,956,
984 2001.
- 985 Visbeck, M., Deep velocity profiling using lowered acoustic doppler current profilers: Bot-
986 tom track and inverse solutions, *Journal of Atmospheric and Oceanic Technology*, *19*,
987 794–807, 2002.
- 988 Visbeck, M., J. Marshall, and H. Jones, Dynamics of Isolated Convective Regions in the
989 Ocean, *Journal of Physical Oceanography*, 1996.
- 990 Waite, A. M., L. Stemmann, L. Guidi, P. H. R. Calil, A. M. Hogg, M. Feng, P. A. Thomp-
991 son, M. Picheral, and G. Gorsky, To the Deep Ocean in Mesoscale Eddies, *Geophysical*
992 *Research Letters*, *43*, 9791—9800, 2016.
- 993 Xing, X., H. Claustre, S. Blain, F. d’Ortenzio, D. Antoine, J. Ras, and C. Guinet, for in
994 vivo chlorophyll fluorescence acquired by autonomous platforms: A case study with in-
995 strumented elephant seals in the Kerguelen region (Southern Ocean, *Limnol. Oceanogr.*,
996 pp. 483–495, 2012.

Figure 1. (a) CTD casts carried out in the Ligurian Sea during the DEWEX winter cruise in February 2013. Stations were distinguished according to the observed mixed layer depth. The right panel shows the trajectory of glider during the concomitant glider mission MOOSE T00-23. Dots are colored according to the mixed layer mean potential temperature observed between February 11 and 17 with the same color scale as in (c). Depth-average currents estimated by the glider are also shown in dark gray. (b) Full-depth shipborne CTD casts during the winter with dark gray profiles corresponding to deeply mixed profiles. The blue profile is a deeply mixed profile carried out in the Ligurian Sea. The SCV core characteristics is indicated by the thick dashed blue line. (c) Glider section along three consecutive Nice–Calvi sections. From top to bottom: potential temperature, practical salinity, chlorophyll-a fluorescence and dissolved oxygen. Black contours are isopycnals and the white line represent the mixed layer depth. On top of these panels, dots show the high-resolution sampling of the glider.

Figure 2. Same as figure 1 but for the MOOSE-GE 2013 summer cruise and the MOOSE T00-25 glider mission carried out in June–July 2013. In (a), the colored dots along the glider trajectory represents the dissolved oxygen concentration with the same scale as in (c). Note that total carbon was measured at the same stations as phytoplankton pigments. In panel (b), the light gray profiles correspond to those carried out in the Ligurian Sea (defined by the black box drawn in (a)), the black profile is the average of all the gray profiles. The blue profile was carried out within the core of a deep eddy that was further sampled by a glider shortly afterward.

Figure 3. Glider sampling of the SCV. (a) Optimal interpolation of the potential temperature at 400 m and 900 m in the eddy centered rotating coordinate framework (i.e. all profiles and depth-average currents from the glider have been rotated around the eddy center according to radial orbital depth-average currents and their observation date). Radial distribution of (b) potential temperature at 900 m and (c) orbital depth-average currents estimated by the glider. The fitted gaussian distribution of orbital velocities is also drawn ($r_0 = 6.3$ km and $v_0 = 12.2$ cm s⁻¹). The geostrophic component of orbital depth-average currents deduced following *Bosse et al.* [2016] is also shown by the light black line. Note that outliers plotted in gray have been excluded prior to the curve fitting. Histograms representing the number of observations in 1 km bins are also shown in upper panels.

Figure 4. Hydrography of the SCV. Radial distribution of (a) potential temperature, (b) practical salinity and (c) dissolved oxygen (DO). Black contours represent potential density in kg m⁻³. All those fields result from the optimal interpolation constrained by the intense glider survey of the first 1000 m depth. Below that depth, area away from the full-depth profiles inside and outside the SCV core have been shaded. Those profiles are also shown as scatter points on top of the analyzed fields. Note that a radial symmetry has been applied for aesthetic and clarity purposes.

Figure 5. Dynamical diagnostics of the SCV. (a) Radial distribution of cyclogeostrophic velocities v_c . The peak orbital velocity is indicated (at $r = 6.1$ km and 700 m depth). Gray contours represent the only cyclostrophic component of orbital velocities. The red line follows peak velocities over depth. The right panel quantifies the percentage ageostrophy over depth: $(1 - \max_z |v_g| / \max_z |v_c|) \times 100$. (b) Relative vorticity normalized by f . The blue line follows the change of sign of the vorticity. The minimum and maximum values are also indicated. The gray lines are contours of strain normalized by f . (c) Radial distribution of the stratification anomaly relative to the background. The gray contours show the smoothed density field used to compute the geostrophic shear and stratification. (d) Radial distribution of the potential vorticity anomaly relative to the background. The red and blue lines are redrawn on this panel. For (c) and (d), the background is defined as the averaged field between 15 and 20 km (see black lines in right panels). In contrast, profile representative of the SCV core is taken as the averaged field between 0 and 5 km (see blue lines in right panels). Note that we have shaded the area below 1000 m depth, as dynamical diagnostics are only constrained by two full-depth CTD casts and a subsequent optimal interpolation.

Figure 6. Horizontal diffusion of oxygen, heat and salt at the rim of the SCV. (a) The gray dots are the individual observations from the glider of dissolved oxygen (*left*), potential temperature (*middle*) and salinity (*right*) at different depths (450 m, 700 m and 950 m, from the top to the bottom). The black line is the average in 1 km bins with error bar showing the standard deviation in each bin. The light colored line represents the tracer distribution at $t = 0$ and the thick line after 4.5 months of diffusion with the diffusion coefficient optimized to fit the observed data. (b) Distribution of diffusion coefficient as a function of depth for the different tracers.

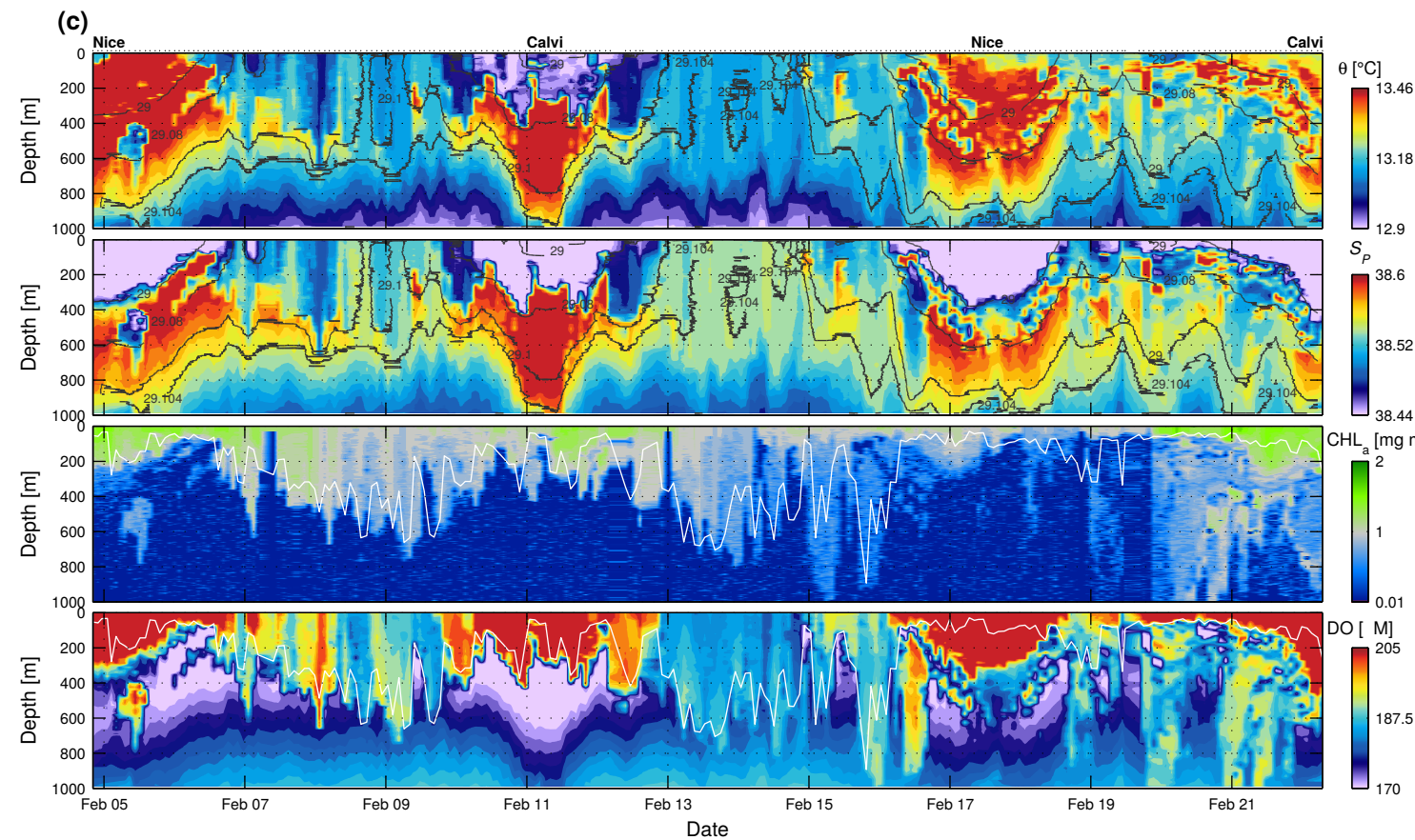
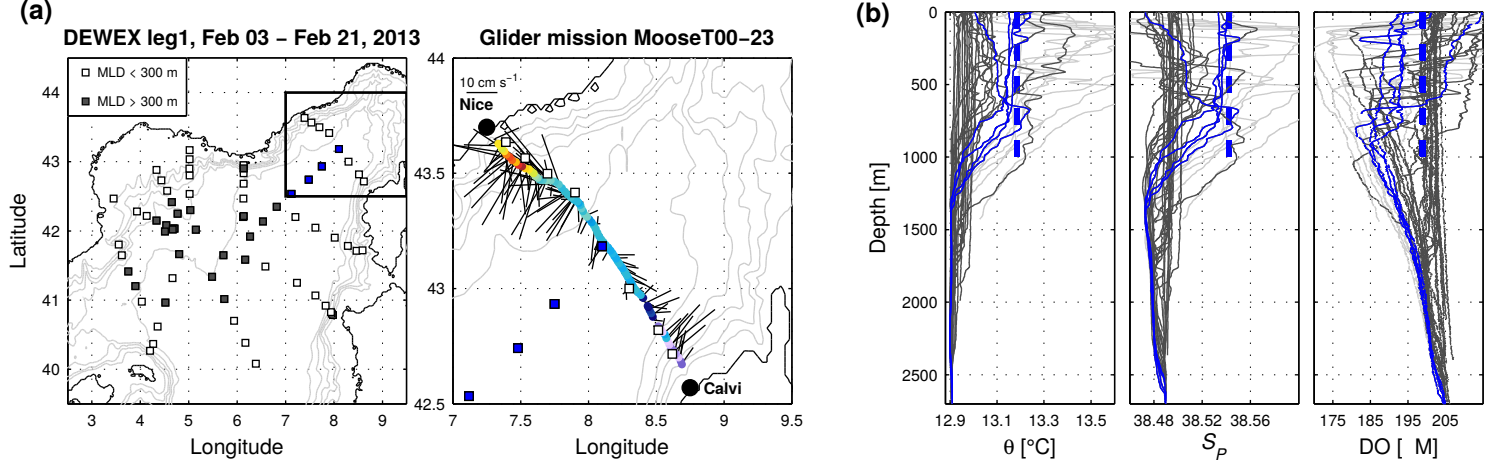
Figure 7. Salinity-Oxygen diagram. The gray lines correspond to background profiles carried out in the Ligurian Sea and the black line is their average. The blue line is the particular profile within the SCV.

Figure 8. Concentrations of the three main nutrients and carbon measured during the MOOSE-GE 2013 cruise: (a) nitrate, (b) phosphate, (c) silicate ions and (d) total carbon. The blue dots show the concentration within the SCV core, while black dots are from the other stations carried in the eastern part of the basin (i.e. longitude $> 6^{\circ}\text{E}$, see the corresponding stations in figure 2-a). The gray shaded area represents the standard deviation of the data.

Figure 9. (a) Bin-averaged section across the eddy of the chlorophyll-a concentration measured by the glider. Black contours show the isopycnals. Note that a radial symmetry has been applied for aesthetic and clarity purposes. Radial distribution of: (b) the chlorophyll-a concentration measured at the deep chlorophyll maximum; (c) the integrated chlorophyll-a concentration over the top 200 m; and (d) the depth of this deep chlorophyll maximum. (e) Chlorophyll-a concentration of three phytoplankton size classes. (f) Primary production associated with each size group. The box plots were constructed using all measurements carried out during the MOOSE-GE 2013 cruise in the eastern part of the basin (i.e. longitude $> 6^{\circ}\text{E}$, see the corresponding stations in figure 2-a). The red mark is the median, the box limits the 25th and 75th percentile and the whiskers show the extension of the dataset. The particular SCV core station is highlighted in blue, as well as the two closest HPLC stations carried out in the Ligurian Sea (Lig1 and Lig2).

Figure 10. Remotely sensed chlorophyll-a concentration at the ocean surface measured by MODIS Aqua scatterometer in June 2013 in the Ligurian Sea. The black dots are the eddy center deduced by *in situ* observations. The white dot is the interpolated eddy center position at the moment the images were taken. A circle of is 12.6 km radius ($= 2r_0$) is drawn to show the eddy outer extension. Note that these are the only good images found from June 13 to July 7.

'Figure 1'.



'Figure 2'.

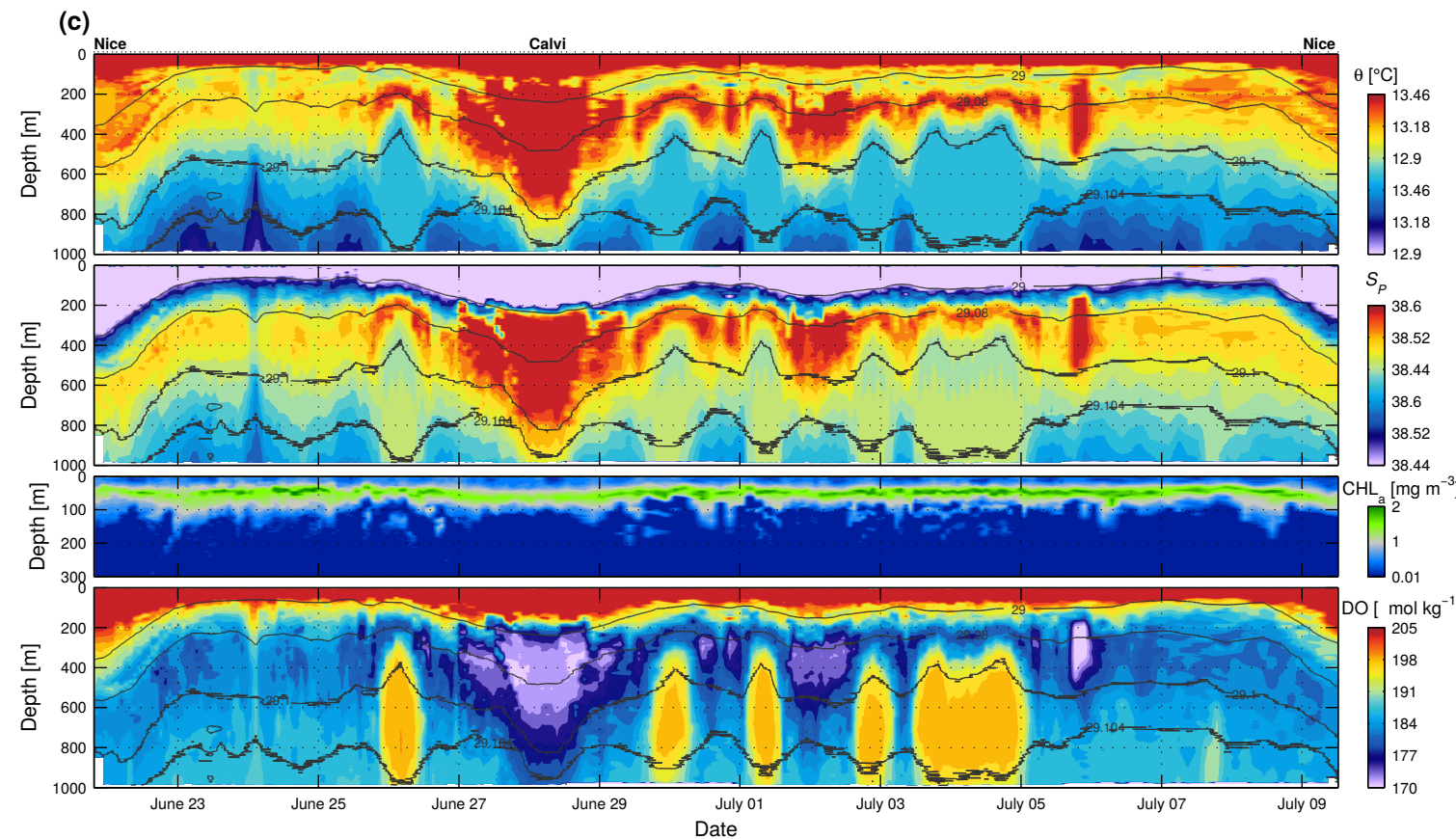
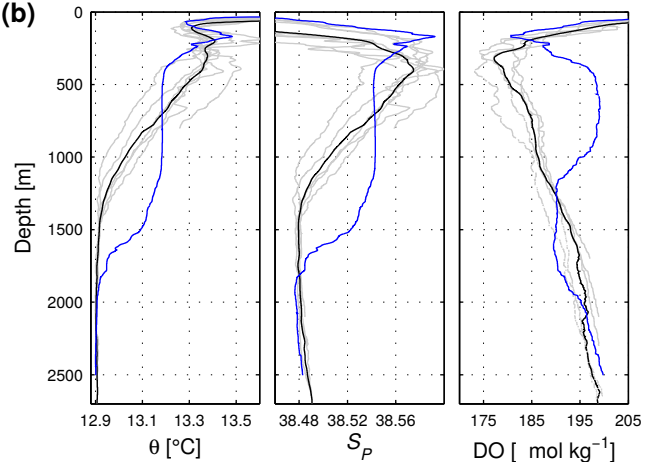
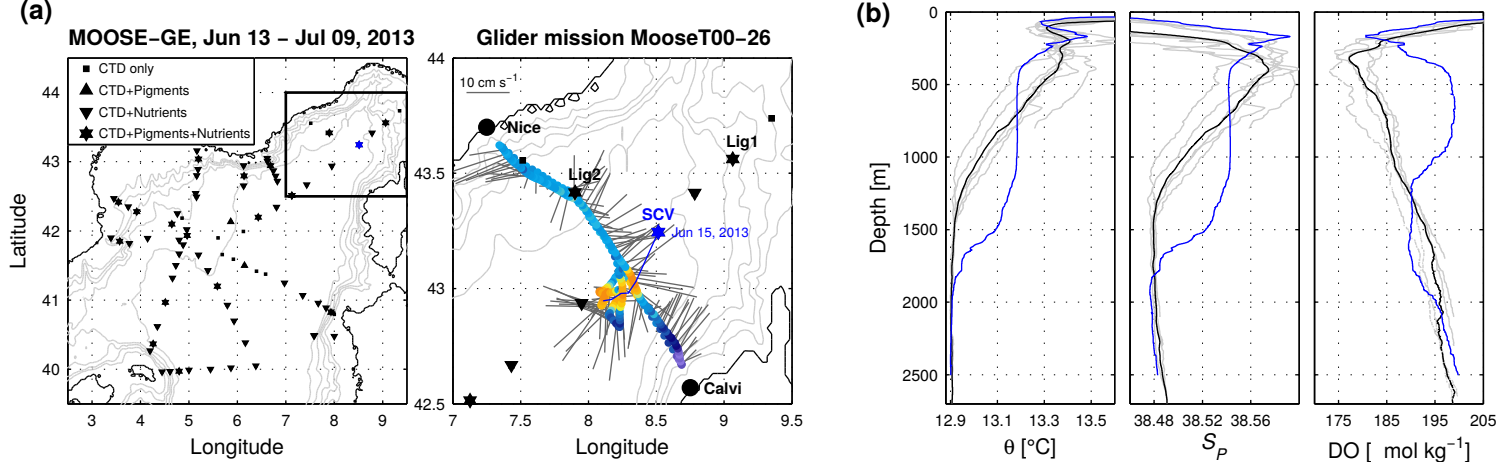


Figure 3.

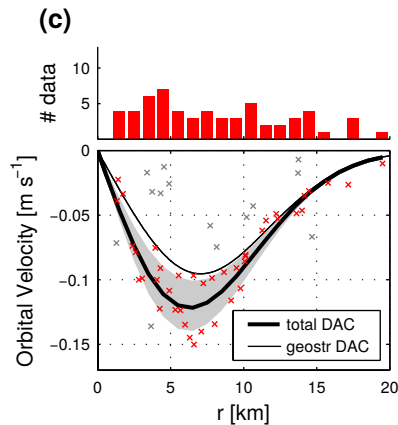
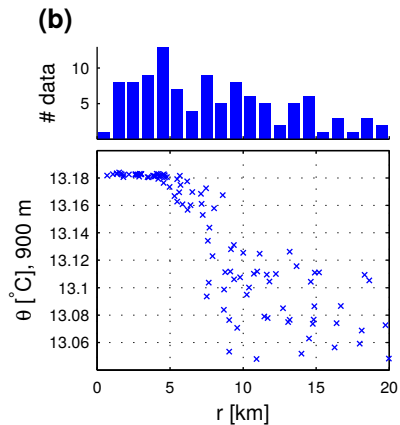
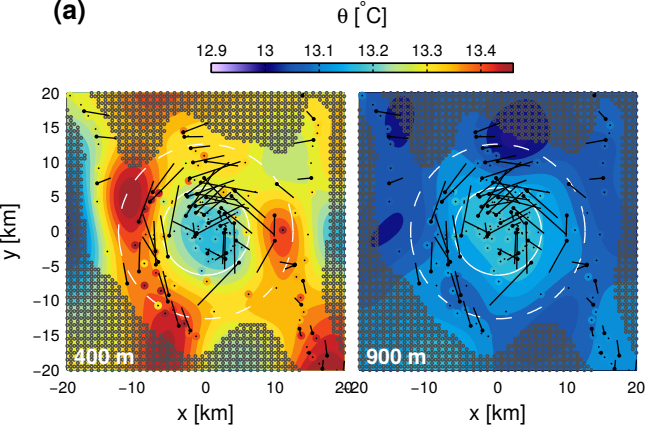


Figure 4.

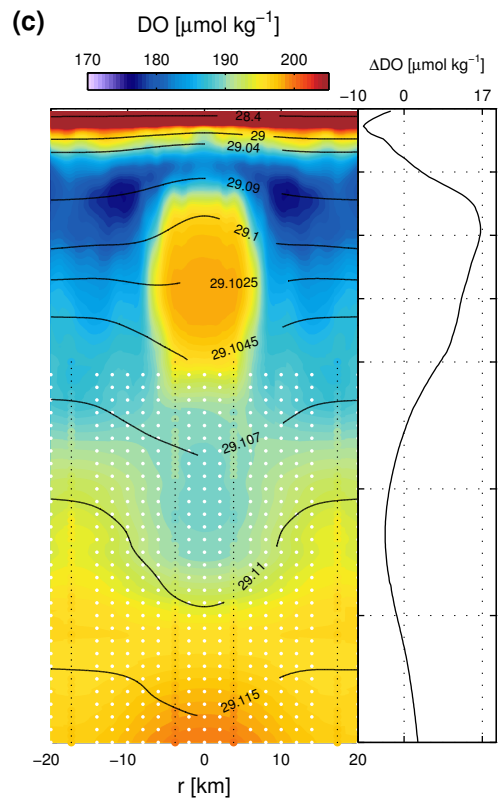
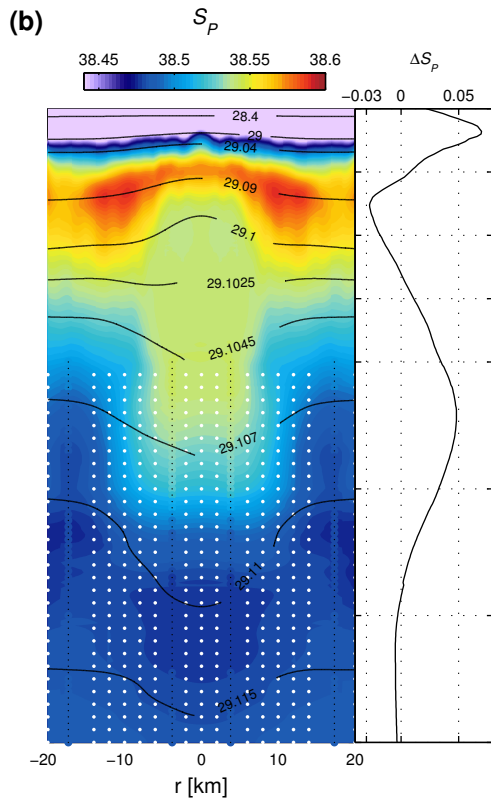
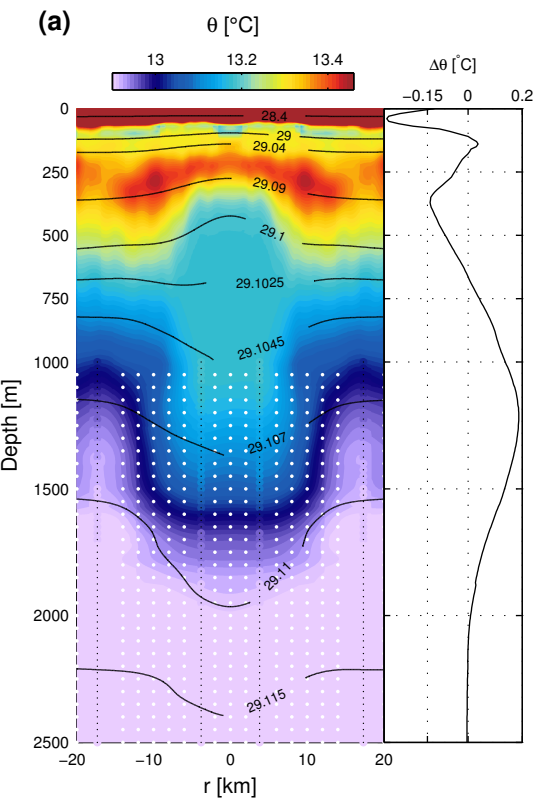


Figure 5.

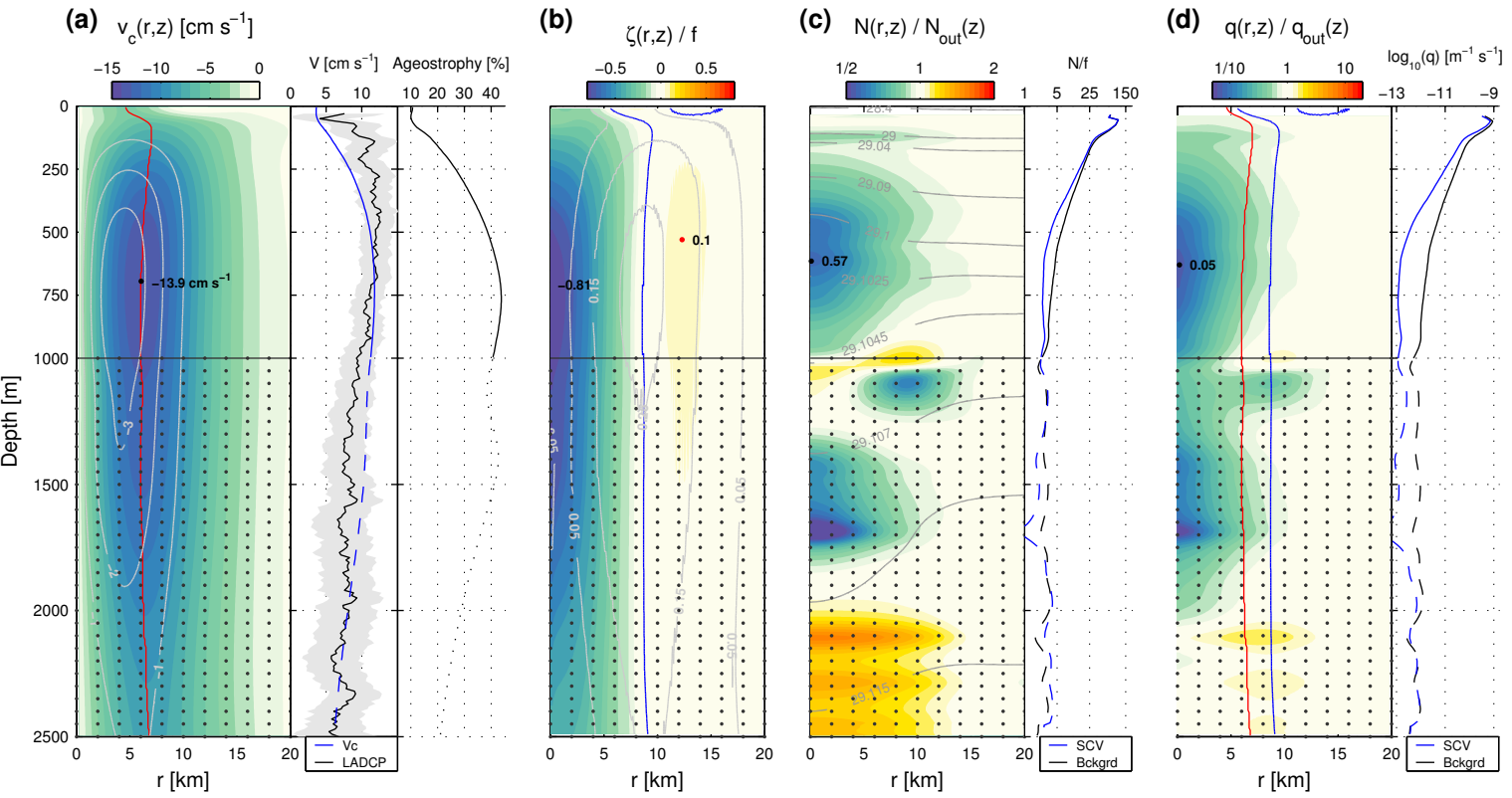


Figure 6.

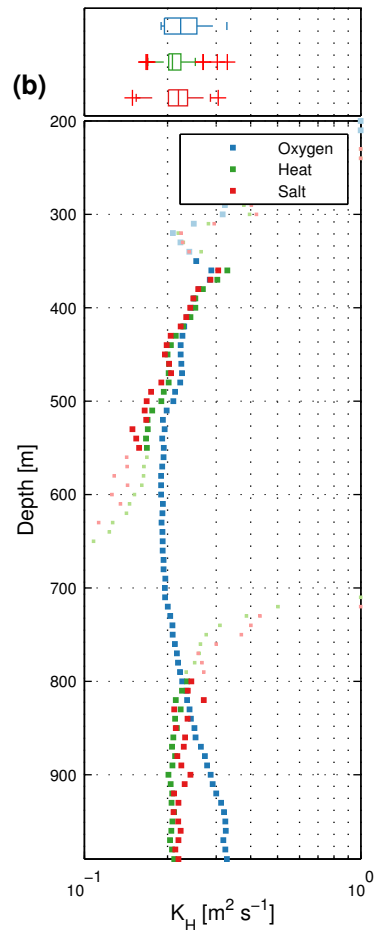
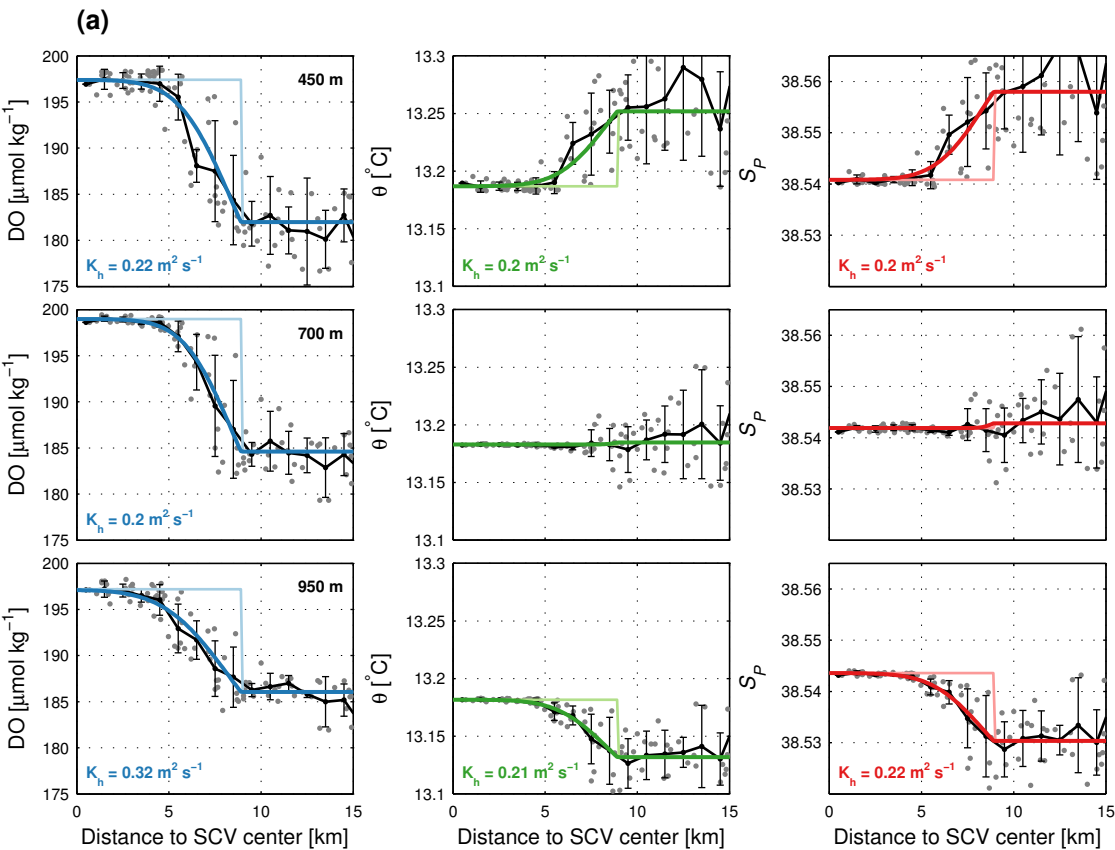


Figure 7.

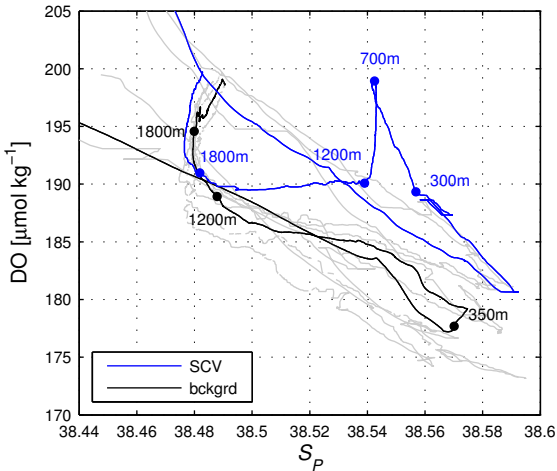


Figure 8.

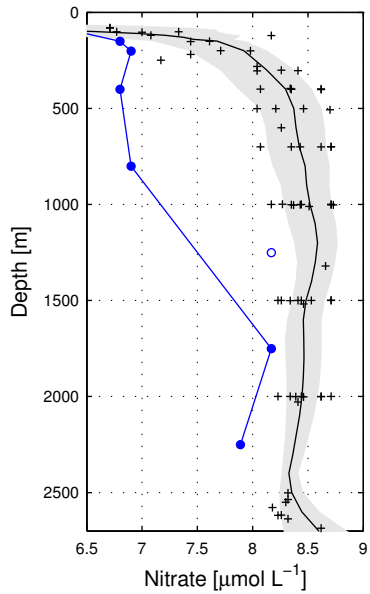
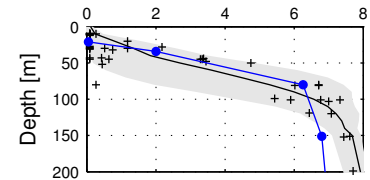
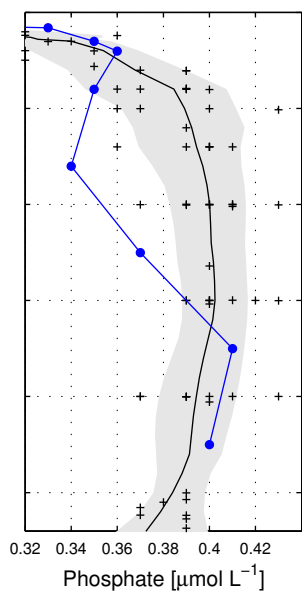
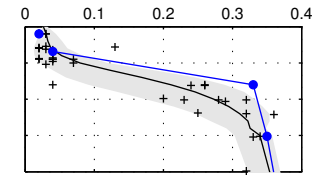
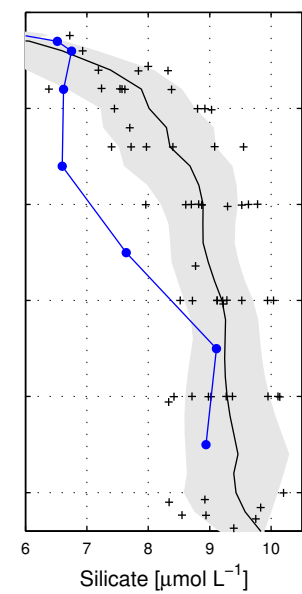
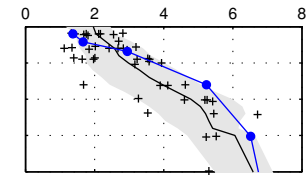
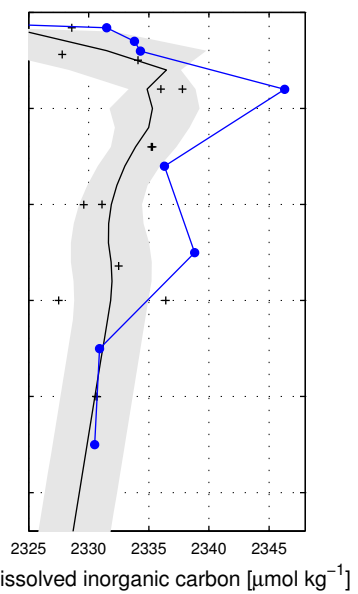
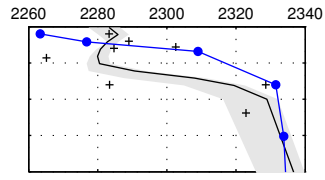
(a)**(b)****(c)****(d)**

Figure 9.

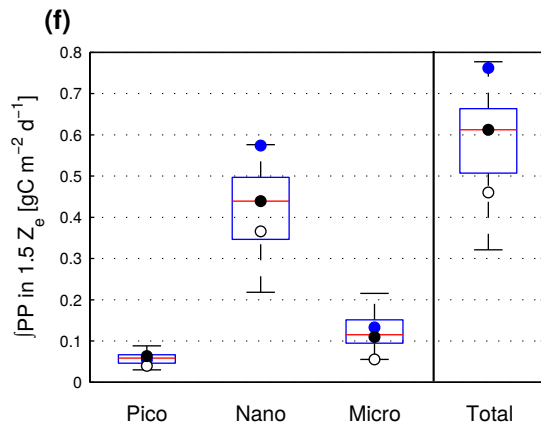
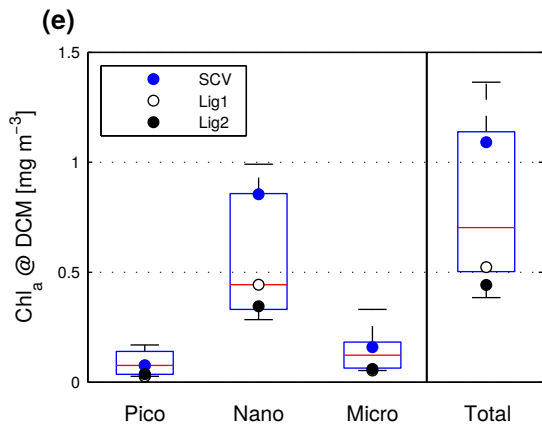
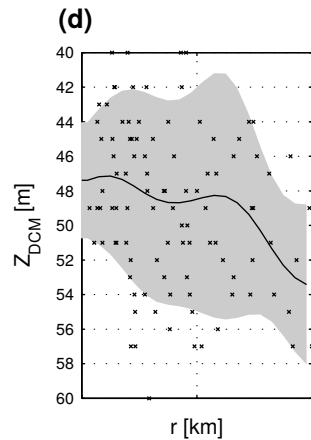
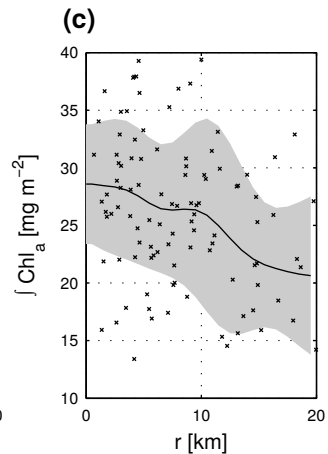
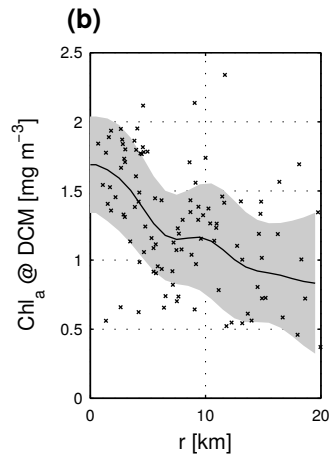
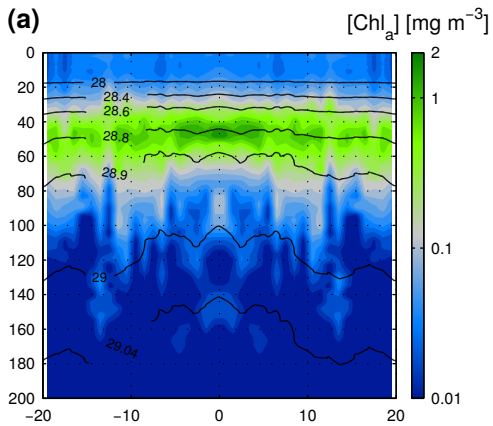


Figure 10.

MODIS Aqua L2 images

